

1 **Exploring inflow wind condition on floating offshore wind turbine**
2 **aerodynamic characterisation and platform motion prediction**
3 **using blade resolved CFD simulation**

4 Yang Zhou¹, Qing Xiao^{1*}, Yuanchuan Liu², Atilla Incecik¹, Christophe Peyrard³, Decheng
5 Wan⁴, Guang Pan⁵, Sunwei Li⁶

6 ¹Department of Naval Architecture, Ocean and Marine Engineering, University of Strathclyde,
7 Glasgow, G4 0LZ, UK

8 ²College of Engineering, Ocean University of China, Qingdao 266100, PR China

9 ³Saint-Venant Hydraulics Laboratory (Électricité de France, ENPC, Cerema), Université Paris-
10 Est, 6 quai Watier, 78400 Chatou, France

11 ⁴Computational Marine Hydrodynamic Lab, State Key Laboratory of Ocean Engineering,
12 School of Naval Architecture, Ocean and Civil Engineering, Shanghai Jiao Tong University,
13 Shanghai 200240, China

14 ⁵School of Marine Science and Technology, Northwestern Polytechnical University, Xi'an,
15 710072, PR China

16 ⁶Division of Ocean Science and Technology, Graduate School at Shenzhen, Tsinghua
17 University, Shenzhen 518055, Guangdong, PR China

18 *Correspondent: qing.xiao@strath.ac.uk

19 **Abstract**

20 The present study is aimed at investigating the effect of turbulent wind and shear wind on the
21 floating offshore wind turbine (FOWT) structure by using a high-fidelity computational fluid
22 dynamics (CFD) method. This method is believed to resolve the wind field around the turbine
23 blades, wake and the near air-wave free-surface regime, allowing us to have a more in-depth
24 examination into both aerodynamic and hydrodynamic of the FOWT. In the present study, the
25 modelling of a coupled aero-hydro-mooring FOWT system is focused on a temporal and spatial
26 variable turbulent wind field by using a time-varying spectrum, which has not been examined
27 for a floating wind turbine. The turbulent wind in the study is generated with Mann's wind
28 turbulence model, while the Von Karman wind spectrum is used to represent wind turbulence.
29 In addition, different wind shears were also examined. We can conclude from this study that,
30 when turbulent wind is present, there are fluctuations in both the rotor thrust and power outputs
31 associated with the non-uniform wake region although the time-mean magnitude is almost the
32 same. In addition, turbulence wind lead to a quicker wake diffusion than time-independent
33 inflow wind. Furthermore, the existence of wind shear results in an even larger decrease in the
34 local minimum thrust/power about 2-6% when the turbine blade is passing in front of the tower.
35 Despite this, under the present wind inflow conditions, the inline surge force, dynamic motion,
36 and the mooring tension of the floater are not significantly affected by either the turbulence
37 wind or the wind shear.

38 *Keywords: Turbulent wind, Computational Fluid Dynamics (CFD), Floating offshore wind*
39 *turbine (FOWT)*

40 **1 Introduction**

41 In recent years, the concept of FOWT has been rapidly developing as it is claimed that these
42 FOWT systems can offer a better solution to wind energy compared to their counterpart

43 onshore wind turbines, for example, Hywind-Scotland [1], the first commercial offshore wind
44 farms achieves 65% of capacity factor, which is much higher than a typical bottom-fixed
45 offshore or onshore wind turbine with a capacity of 30%-45%. Numerical analysis is one of
46 many key tools during the initial FOWT design stage. Through the application of numerical
47 analysis, we are able to predict the aero/hydrodynamic performance of a coupled FOWT
48 system. Nonetheless, the main challenge is being able to replicate these results under real
49 environmental wave and wind conditions.

50 Some of the most commonly used methods accustomed to analyse the aerodynamic of a wind
51 turbine include: low-cost Blade Element Method (BEM) and high-fidelity, high-cost
52 Computational Fluid Dynamics (CFD). Due to the fact that CFD allows us to directly solve the
53 fluid flow governing equations, we are able to use it to produce detailed flow variables in both
54 the time and spatial domains so that the transient aerodynamic loading on the tower, turbine
55 blade, and the wind wake structure can all be well resolved. For a typical FOWT, the operating
56 wind speed and the size of the FOWT contribute to changing the airflow into turbulent regime.
57 This means that CFD modelling for a FOWT must factor in the turbulent feature. There are
58 three general approaches for turbulence modelling. These are: Large Eddy Simulation (LES),
59 Direct Numerical Simulation (DNS) and Unsteady Reynolds-Average Navier-Stokes
60 (URANS). Recently, a hybrid model named Improved Delayed Detached Eddy Simulation
61 (IDDES) is developed [2], in which URANS is employed in the near wall treatment and LES
62 model is used in the far field. Due to the fact that IDDES predicts more accurate solutions on
63 wind turbine aerodynamics while owes a lower computational cost than the LES, it has been
64 applied in several research areas including wind turbine. However, a quick review on the
65 IDDES [3-5] papers for wind turbine investigation indicated that all studies are focused on
66 either a bottom-fixed wind turbine or a floating system with prescribed pitch and surge motions.
67 Therefore, the *free-motion* of floating structure is entirely excluded in their studies. This is also

68 an indicator that the applicability and reliability of IDDES on the numerical prediction of ocean
69 waves and the wave-structure interaction problems have not been fully validated and verified.
70 Therefore, out of these approaches, URANS is considered as the most efficient method due to
71 its relatively low computational cost while also having reasonably good predictions for the
72 time-mean variables.

73 As of right now, most FOWT turbulent CFD analysis simplifies the problem by assuming a
74 uniform and constant incoming wind field. However, in a non-controlled environment, the real
75 wind field is much more unpredictable and considered as a stochastic process, which varies in
76 both temporal and spatial domains. To allow us to replicate conditions of wind turbulence such
77 that they reflect a real life scenario, spectral methods are commonly used so that we can
78 reproduce such a turbulent wind field. Here, the given wind spectrum is broken down into a set
79 of turbulent components with various wave numbers and frequencies. One of the commonly
80 used approaches is addressed by Veers [6] based on the observation of Atmospheric Boundary
81 Layer (ABL) spectra to provide three-dimensional turbulent components over homogeneous
82 terrain. This method has been adopted in the National Renewable Energy Laboratory (NREL)
83 TurbSim code [7]. It has also been coupled alongside NREL FAST [8] to model the aero-
84 hydro-servo-mooring FOWT system under turbulent inflow conditions. Another technique
85 used is the Mann wind turbulence model [9] which utilizes a velocity spectral tensor to predict
86 a second-order three-dimensional fully turbulent field. Mann's method is able to accurately and
87 efficiently simulate the homogeneous inflow and ABL turbulence [10, 11].

88 Previous studies into the understanding of the impact that turbulence has on a wind turbine
89 began onshore before progressing onto offshore fixed and floating systems. Li et al. [12]
90 utilized the Mann wind turbulence model to analyse a bottom-fixed wind turbine aided by CFD
91 code (CFDship-Iowa). The study found that the wake diffusion would increase in the presence

92 of turbulence. By using a simple actuator line theory and LES modelling, Troldborg et al. [13]
93 investigated the effect of both uniform and turbulent wind conditions on a bottom-fixed wind
94 turbine. This was also done using the Mann wind turbulence model and a simplified wind
95 turbine model. His study revealed that when wind turbulence is present, the wake is found to
96 be more unstable than if turbulence was absent. As we get closer to the turbine rotor, we can
97 see this effect become increasingly more prominent in this region. In addition to this, the study
98 found that the disparity under various wind turbine-modelling methods is negligible. Knowing
99 that the wind turbulence will have a significant impact on the wind farm performance, Olivares
100 et al. [14] analysed the modelling of homogeneous turbulence inflow in the turbine wake
101 through utilizing actuator disk (AD) theory and LES modelling. His study showed that the
102 velocity field within the wake region becomes uniform whilst the turbulence kinetic energy
103 increases behind the AD model. This effect can be attributed to the existence of the AD edges.
104 In addition to this, Chivaae et al. [15] performed a study in which he investigated a 2D air-foil
105 under turbulent wind by using the LES method and the Sub-Grid Scale (SGS) model. His
106 research extended to the fixed wind turbine wake under turbulent wind. We can see from his
107 work that the blade tip vortices could be captured accurately under fine mesh resolution.
108 Contrary to this, the coarse mesh provides rather poor wake predictions. Moreover, Grinderslev
109 et al. [16] compared the onshore wind turbine aerodynamic performance considering the
110 turbine flexibility under turbulent inflows using LES and IDDES models, his study revealed
111 that there is no significant difference between both methods on the prediction of separate flows
112 and blades deflection.

113 Moving from onshore to offshore floating wind turbine concepts, recent research conducted by
114 Li et al. [17] focuses on a semi-submersible NREL 5 MW FOWT using the BEM tool under
115 different wind inflow conditions. His results show that the existence of a turbulent wind field
116 led to a very unstable thrust force and power. By using a high-fidelity LES method to solve the

117 wind turbine aerodynamic and a low-fidelity potential theory based method to predict the
118 floating platform hydrodynamic, Doubrawa et al. [18] conducted an investigation on the
119 hydrodynamic loads of a Hywind Spar floating wind turbine under turbulent wind conditions
120 with the use of Simulator for Offshore Wind Farm Applications (SOWFA) and NREL FAST.
121 Their results demonstrated that with the aid of the stochastic wind turbulence models, the
122 fatigue loads were overestimated at low wind speeds (0-8m/s) but underestimated at high wind
123 speeds (over 25m/s).

124 Other than the turbulence wind nature mentioned above, in a wind farm area in real life, wind
125 field shear layer is regarded as another key factor which will have an impact on the wind turbine
126 aerodynamic. The onshore wind turbine can be seen to be greatly influenced by this factor due
127 to the boundary layer development on land. Dolan and Lehn [19] performed a wind shear study
128 on an onshore wind turbine with a comprehensive model based on analytical formulations.
129 They concluded that wind shear resulted in a slight reduction of the power of the rotor
130 compared to uniform wind. This reduction then became more significant when exposed to
131 tower shadow effects [20]. These effects could also be seen in the work conducted by Wen et
132 al. [21] through using the Free Vortex Method (FVM). Gould et al. [22] discovered the pitch
133 moment difference of the onshore wind turbine subjected to a series of shear winds based on a
134 momentum-based method. Their research revealed that when the wind shear layer thickness
135 was gradually increased, a higher shear-induced pitch moment could be seen and caused further
136 fatigue damages to the wind turbine. Recent research by Li et al [17] using BEM to examine
137 the wind shear on FOWT concluded that, although wind shear has a minor influence on the
138 total power outputs of the rotor, the local aerodynamic loads fluctuations caused by wind shear
139 produced additional fatigue damage loads onto the root of blade.

140 Admitting that the impact of the inflow wind turbulence or wind shear on the aerodynamic
141 performance of the wind turbine have been examined in aforementioned studies, however, most
142 of them are conducted either on a bottom-fixed offshore wind turbine or an onshore wind
143 turbine. For a floating wind turbine, the effects of the inflow wind conditions may play an
144 important role and reveal new characteristics near the wave-air surface, and also the *floating*
145 moored structure caused by the aero-hydro-mooring coupling. These features are entirely
146 excluded for a fixed wind turbine or for a prescribed platform motions as studies in [23, 24].

147 Although some of the recent research has considered the FOWT subjected to turbulent wind
148 conditions, those research regarding the effects of turbulent inflow and shear wind on the wind
149 turbine used simplified methods to model the effect on the blades, such as BEM or AL/AD
150 models. In addition, some researchers applying a prescribed surge/pitch motion onto a FOWT
151 tower to represent the motion of a floater. In addition, as FOWT is a complex system, it is hard
152 to study such fully coupled aero-hydro-mooring problem using any laboratory testing to
153 combine all factors into consideration. i.e., turbulent wind aerodynamics, ocean wave
154 hydrodynamics, floating structure motion response, and mooring system. Therefore, at current
155 stage, the numerical modelling plays a significant role on FOWT investigations for identifying
156 the main parameter matrix and guiding the design of laboratory testing.

157 The current study investigates the behaviour of a FOWT under the influence of a turbulent
158 wind field generated by the incoming wind spectrum in addition to the shear wind field. As
159 mentioned earlier, the blade-resolved flow examination in addition to the motion capturing of
160 free floater, allow us to understand both the aerodynamic and hydrodynamic details of FOWT.
161 However, these have not been accounted for in previous studies conducted. The current
162 perception is that turbulent wind may have an effect on both the unsteady aerodynamic loading
163 of the wind turbine and the hydrodynamic response of the floater. The existence of wind shear

164 may cause variance in the local aerodynamic characteristics and the pitch moment of the
 165 FOWT. These effects may result in an overall performance change of the turbine. The aim is
 166 achieved by using our in-house hydro-aero-mooring CFD tool [25-28], which is able to fully
 167 resolve the flow field details around the turbine blades and the area where wave-air has strong
 168 interaction with the free surface. The Mann wind turbulence model is also adopted to replicate
 169 the turbulent wind. The magnitude and spatial distribution of the turbulence are put in as
 170 boundary condition inputs to the CFD solver. The modelling of a FOWT under regular wave
 171 conditions is then carried out in our numerical wave tank. After this, the aero/hydrodynamic
 172 responses are computed before being compared to the values predicted by the BEM tool.

173 **2 Numerical Methodology**

174 **2.1 Flow solver**

175 **2.1.1 Governing equations of fluid flow**

176 The open source Computational Fluid Dynamics framework OpenFOAM [29] is applied as the
 177 flow solver for the duration of the coupled FOWT simulation. The governing continuity and
 178 momentum equations for a transient, incompressible flow can be written as,

$$\nabla \cdot \mathbf{U} = 0 \quad (1)$$

$$179 \quad \frac{\partial \rho \mathbf{U}}{\partial t} + \nabla \cdot (\rho(\mathbf{U} - \mathbf{U}_g)\mathbf{U}) = -\nabla P_t - \mathbf{g} \cdot \mathbf{x} \nabla \rho + \nabla(\mu_{eff} \nabla \mathbf{U}) + (\nabla \mathbf{U}) \cdot \nabla \mu_{eff} + \mathbf{f}_\sigma \quad (2)$$

180 where \mathbf{u} and \mathbf{u}_g represent the velocity of the flow field and grid nodes in Cartesian coordinates,
 181 respectively; ρ refers to the mixed density of water and air, \mathbf{g} denotes the gravity acceleration;
 182 $P_t = P - \rho \mathbf{g} \cdot \mathbf{x}$ is the dynamic pressure obtained by the total pressure P minus the hydrostatic
 183 pressure $\rho \mathbf{g} \cdot \mathbf{x}$; We can use the formula $\mu_{eff} = \rho(v + v_t)$ to calculate the effective dynamic

184 viscosity, in which ν and ν_t are the kinematic and eddy viscosity respectively; \mathbf{f}_σ represents
 185 the surface tension.

186 **2.1.2 Turbulence modelling**

187 The $k-\omega$ SST (Shear Stress Transport) turbulent model is used to account for a high Reynolds
 188 number. This may reach values as high as $Re=10^7$ for a typical wind turbine. As indicated by
 189 previous studies, the $k-\omega$ SST turbulence model [30] is made up from a combination of the
 190 standard $k-\omega$ model and the $k-\varepsilon$ model. To be specific, it combines the standard $k-\omega$ model
 191 found near the structure boundary layer and changing to the $k-\varepsilon$ model in the far-field. This
 192 design shows its strengths in adverse pressure gradients and predicting separating flow.

193 For the governing equations for turbulent kinetic energy (TKE) k and the specific dissipation
 194 rate ω , we can show that,

$$\frac{\partial \rho k}{\alpha t} + \nabla \cdot (\rho \mathbf{U} k) + \nabla \cdot (\Gamma_k \nabla k) + \widetilde{P}_k - D_k = 0 \quad (3)$$

$$\frac{\partial \rho \omega}{\alpha t} + \nabla \cdot (\rho \mathbf{U} \omega) + \nabla \cdot (\Gamma_\omega \nabla \omega) + P_\omega - D_\omega + Y_\omega = 0 \quad (4)$$

195 where Γ_k and Γ_ω denotes the effective diffusivity of the turbulent kinetic energy k and the
 196 specific dissipation rate ω respectively; \widetilde{P}_k and P_ω refers to the turbulence production terms,
 197 and D_k and D_ω are the turbulence dissipation terms; Y_ω is the cross-diffusion term introduced
 198 by blending the standard $k-\omega$ and $k-\varepsilon$ models.

199 **2.1.3 Free surface modelling**

200 To allow capturing of the air-water free surface, the Volume of Fluid (VOF) method [31] is
 201 applied in OpenFOAM, in which the free surface is represented by the volume fraction α . For
 202 a two-phase air-water fluid flow, the volume fraction is distributed as follows,

$$\begin{cases} \alpha = 0, \text{air} \\ \alpha = 1, \text{water} \\ 0 < \alpha < 1, \text{free surface} \end{cases} \quad (5)$$

204 The governing equations of the volume fraction variable α follows,

$$\frac{\partial \alpha}{\partial t} + \nabla \cdot \mathbf{u}\alpha + \nabla \cdot [\mathbf{u}_r(1 - \alpha)\alpha] = 0 \quad (6)$$

206 In order to capture the free surface accurately, a bounded compression method with an
207 additional compression term on the left-hand side of the transport equations has to be
208 introduced which only functions near free surface due to the inclusion of $(1 - \alpha)\alpha$, where
209 $\mathbf{u}_r = \mathbf{u}_{\text{water}} - \mathbf{u}_{\text{air}}$ is an artificial velocity field, and used to compress the interface.

210 For a multiphase flow problem, the volume fraction of each liquid is used as the weighting
211 factor to calculate the mixture properties. Listed below are the equations for the density and
212 the viscosity,

$$\rho = \alpha\rho_l + (1 - \alpha)\rho_g \quad (7)$$

$$\mu = \alpha\mu_l + (1 - \alpha)\mu_g \quad (8)$$

213 where the subscripts l and g refer to the liquid and gas respectively.

214 **2.1.4 Wave generation and absorbing**

215 To generate regular waves in our numerical wave tank, an open-source toolbox “waves2Foam”
216 [32] has to be used. A new boundary condition at the inlet boundary was implemented in the
217 OpenFOAM to generate different types of numerical waves based on the relevant wave theories.
218 In addition, the relaxation zone was adopted to provide better wave quality whilst also avoiding
219 wave reflection in the absorbing zones. This technique is applied at both the inlet and outlet
220 boundaries in the numerical wave tank. The main functions of the relaxation zones are specified
221 as follows,

$$\alpha_R(\chi_R) = 1 - \frac{\exp(\chi_R^{3.5}) - 1}{\exp(1) - 1} \quad (9)$$

$$\phi_R = \omega_R \phi_R^{computed} + (1 - \omega_R) \phi_R^{target} \quad (10)$$

222 where ϕ_R represents either the velocity or volume fraction of water α ; the definition of χ_R is
 223 that the weighting functions α_R is always equal to 1 at the interface between the non-relaxed
 224 computational domain and the relaxation zones, while χ_R refers to a value between 0 and 1.

225 In the present work, the stokes second order regular wave theory is adopted in the present study
 226 which is widely used in ocean waves modelling. The surface elevation can be represented into
 227 the time domain by the following equation,

$$\eta(x, t) = A \cos \delta + \frac{A}{16} \frac{Agk}{\omega} \frac{\cosh kh}{\sinh^3 kh} \cosh(2kg + 2) \cos 2\delta \quad (11)$$

228 where A represents the wave amplitude; ω is the angular frequency; φ denotes the wave
 229 phases; h refers to the water depth and k is the wave number.

230 The vertical and horizontal velocities w and u implemented to the inlet boundary are given by,

$$w(x, t) = \frac{Agk}{\omega} \frac{\sinh k(z + h)}{\cosh(kh)} \sin \delta + \frac{3}{4} \frac{Agk}{\omega} \frac{AH}{2\lambda} \frac{\sinh 2k(z + h)}{\cosh^4(kh)} \sin 2\delta \quad (12)$$

$$u(x, t) = \frac{Agk}{\omega} \frac{\cosh k(z + h)}{\cosh(kh)} \cos \delta + \frac{3}{4} \frac{Agk}{\omega} \frac{AH}{2\lambda} \frac{\cosh 2k(z + h)}{\cosh^4(kh)} \cos 2\delta \quad (13)$$

231 g is the gravitational acceleration; z refers to the vertical length measured upwards from the
 232 still water level; h is the water depth and λ representing the wavelength.

233 2.1.5 Mooring line modelling

234 A mooring system analysis module is implemented into the coupled aero-hydro-mooring
 235 system under the CFD framework [26], where both the quasi-static [33] and the dynamic
 236 mooring line modules are developed. The dynamic method is then adopted in order to capture
 237 more accurate results, as we take into account any dynamic effects which include inertial forces
 238 compared with quasi-static mooring line modelling.

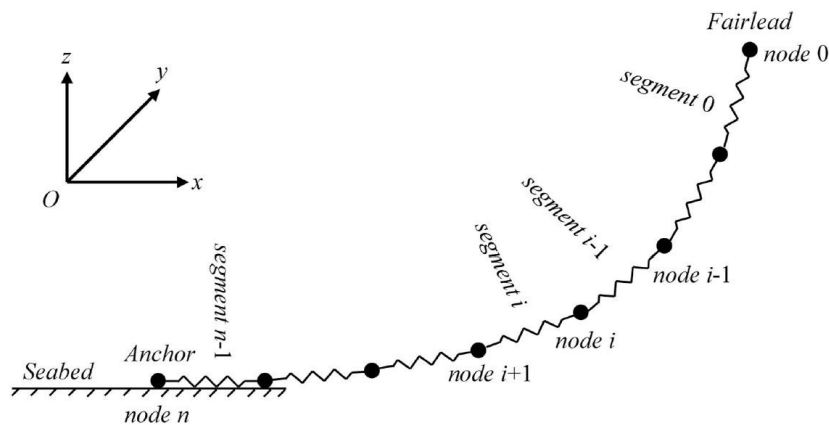


Figure 1 3D Lumped-mass dynamic mooring line modelling

239 Typically, the mooring lines are not directly simulated in the CFD computational domain.
 240 Instead, the tension loads of the mooring lines are added as constraints on the patches of the
 241 floater onto the computational mesh. In order to capture the tension loads subjected to the
 242 mooring lines, a 3D-lumped mass method is adopted to perform the dynamic mooring line
 243 behaviour. The sketch of the dynamic mooring line modelling is shown in Figure 1.

244 In a 3D-lumped mass model, the mooring lines are discretized into $n+1$ nodes (concentrated
 245 masses) which are connected by n springs (massless segments). All the nodes have to satisfy
 246 the equilibrium equations and elongation equations both in the horizontal and vertical
 247 directions. At the beginning of the simulations, the initial tension forces at the first segment
 248 connected with the platform are specified as the estimated total weight of the mooring lines in
 249 water. In addition, the positions of mooring anchor are always checked at each unsteady time
 250 step to guarantee the predicted mooring anchor position is consistent with the constraints

251 imposed by the anchor. If the convergence criterion is satisfied of the error functions, then the
252 tension loads of each segment is determined.

253 In order to calculate the hydrodynamic loads on the mooring lines exerted by the fluid flow
254 (which is neglected during the CFD modelling), Morison's equations [34] are adopted in the
255 mooring system analysis module. Both the drag force and virtual mass force (inertial force) is
256 computed. This is done firstly for line segments and then transformed to the adjacent nodes.

257 2.2 Turbulent wind modelling

258 To solve the problem of turbulent wind modelling, the Mann [9] method is implemented into
259 the current flow solver. As we can see in Mann's method, the Mann wind turbulence box is
260 based off the construction of a velocity-spectrum tensor (ϕ_{ij}) of a neutral atmospheric
261 boundary layer (ABL). The turbulence field is then reproduced with second-order statistics
262 derived from two things, either from the covariance tensor or from its Fourier transform.
263 Generally, they are relevant to the spectral tensor (i.e. Von Karman tensor in the present study).
264 However, the stochastic velocity field $u(x)$ does not have a direct Fourier transform as it is
265 unable to be integrated over the space. Mann's velocity field can be represented in terms of a
266 generalized Fourier-Stieltjes integral

$$u(x) = \int e^{i\kappa \cdot x} d\mathbf{Z}(\kappa) \quad (14)$$

267 In which κ represents the wave number vector and the integration of κ covers all the wave
268 number space which makes up the velocity field; $\mathbf{Z}(\kappa)$ refers to a complex orthogonal
269 stochastic process. We can then use this process to calculate the velocity-spectrum tensor ϕ_{ij}

$$\phi(x)_{ij} d\kappa_1 d\kappa_2 d\kappa_3 = \langle d\mathbf{Z}_i^*(\kappa) d\mathbf{Z}_j(\kappa) \rangle \quad (15)$$

270 where * stands for the conjugate and $\langle * \rangle$ represents averaging. Because the velocity-spectrum
 271 tensor ϕ_{ij} is related to its covariance three-dimensional energy spectrum, if the flow is thought
 272 to be incompressible, the spectral tensor can then be given by the formula,

$$\phi_{ij}(\kappa) = \frac{E(\kappa)}{4\pi\kappa^4} (\delta_{ij}\kappa^2 - \kappa_i\kappa_j) \quad (16)$$

273 The Von Karman spectrum [35] is selected for use in the current study as it is one of the
 274 recommended energy spectrums in the International Electrotechnical Commission (IEC). This
 275 is given as,

$$E(\kappa) = \alpha\varepsilon^{2/3}L^{5/3} \frac{L^4\kappa^4}{(1 + L^2\kappa^2)^{17/6}} \quad (17)$$

276 where α is the Kolmogorov constant, ε is the rate of dissipation of turbulent kinetic energy
 277 (TKE) and L represents a length scale. As it is currently impossible to measure the energy
 278 spectrum experimentally, we must utilize one-dimensional spectra which can be derived after
 279 following the relationship with three-dimensional spectrum [36]. The one-dimensional Von
 280 Karman spectrum can be expressed as follows, for the spectrum relating to longitudinal
 281 direction,

$$F_1(\kappa_1) = \frac{9}{55} \alpha\varepsilon^{2/3}L^{5/3} \frac{1}{(1 + L^2\kappa_1^2)^{5/6}} \quad (18)$$

282 For the spectrum of transversal direction ($i=2,3$),

$$F_i(\kappa_1) = \frac{3}{110} \alpha\varepsilon^{2/3}L^{5/3} \frac{3 + 8L^2\kappa_1^2}{(1 + L^2\kappa_1^2)^{11/6}} \quad (i = 2,3) \quad (19)$$

283 **2.3 Implementation wind turbulence to flow solver**

284 The Mann wind turbulence method described above has been built into our coupled hydro-
 285 aero-mooring CFD solver. We can see how it is implemented into the simulation in Figure 2.
 286 There are three main steps to this. Firstly, the homogeneous isotropic turbulence wind field has
 287 to be generated. Fast Fourier transform is utilized to compute the velocity field with the given
 288 one-dimensional spectra, i.e., equations (18) & (19). After doing so, we are able to generate a
 289 three-dimensional field with this data. Taylor’s frozen hypothesis is used to transfer time series
 290 into space series. Based on this, velocities are extracted from different sections of the Mann
 291 wind turbulence box, and various time-domain results can be obtained along a transversal plane
 292 in the Mann box. The relationship between a longitudinal dimension and time is given as,

$$x = L_1 - U_{mean}t \tag{20}$$

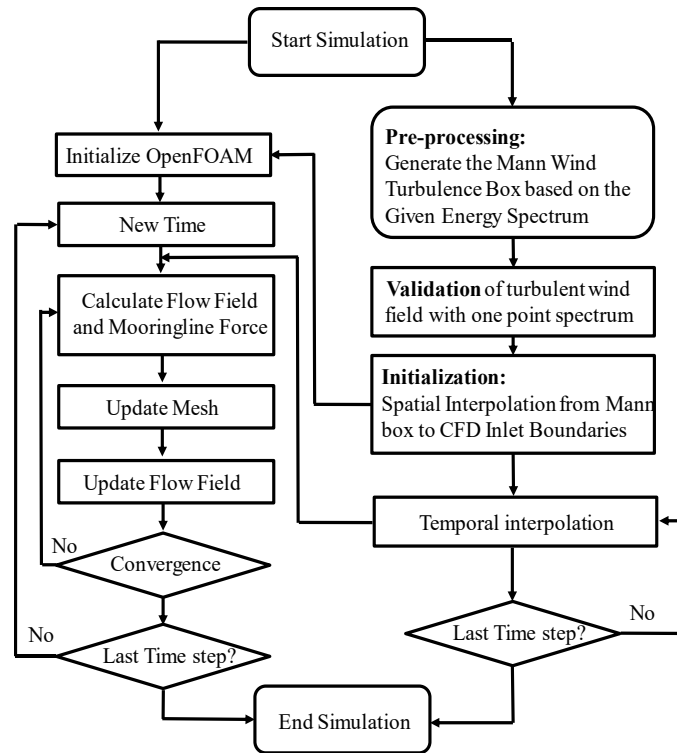


Figure 2 Layout of the implementation of Mann model to OpenFOAM

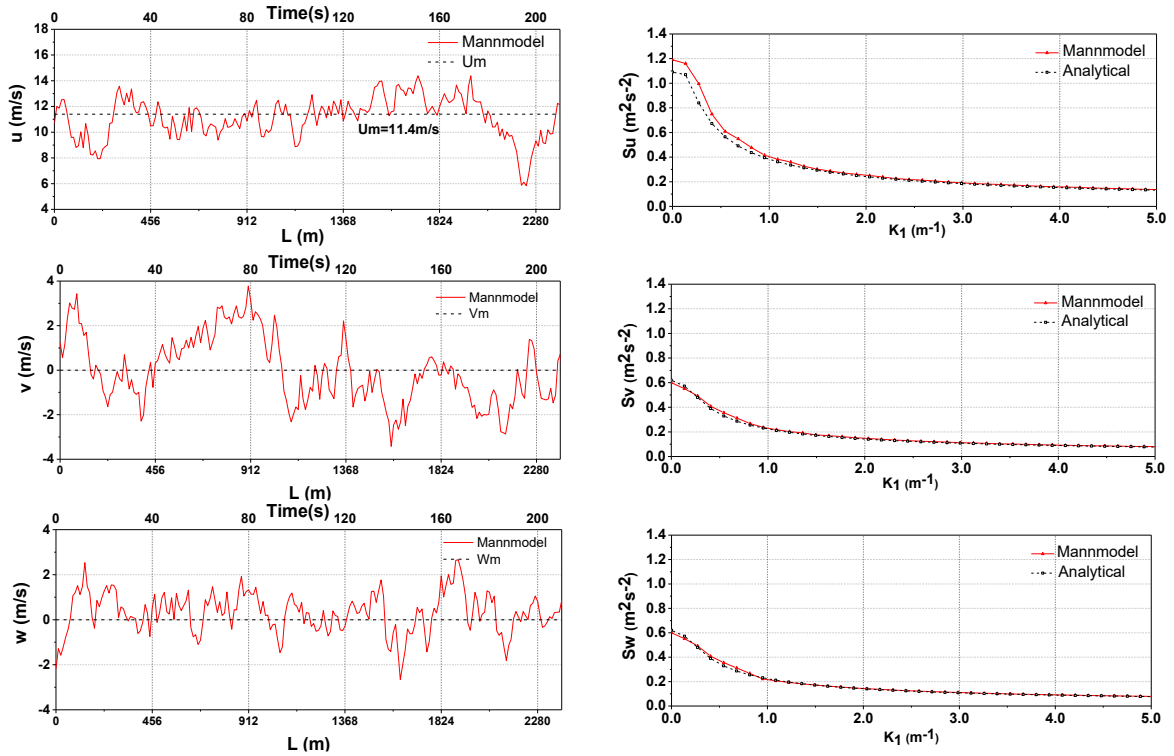


Figure 3 Mann model validation left: velocity distribution along three directions at hub location; right: one-dimensional velocity spectra for each velocity component computed from Mann model

294 where L_1 is the longitudinal dimension of the Mann wind turbulence box and U_{mean} stands for
 295 the mean wind velocity at a specific turbine hub height. The generated turbulence wind field
 296 has to be evaluated against the given wind power spectrum first before they are inserted as the
 297 wind turbulent boundary conditions onto the CFD computational domain. Because the CFD
 298 mesh is finer than the discretized wind field in Mann wind turbulence box, a trilinear
 299 interpolation is required. This allows us to obtain all relevant turbulent velocities at the CFD
 300 mesh along the inlet boundary. Another key factor is that as the unsteady CFD modelling time
 301 step is significantly shorter compared to the time step used for the turbulent wind field
 302 generation, a similar time interpolation is also required.

303 3 Validation and Verification

304 3.1 The implementation of Mann wind turbulence model

305 The study conducted below validates the generation of the turbulence wind field based on
 306 Mann’s algorithm. Firstly, the results are compared against the one-point velocity spectra,
 307 previously defined in Equations (18) and (19). The mean velocity is established as the rated
 308 wind speed at 11.4m/s of an NREL 5 MW wind turbine. The Mann wind turbulence box domain
 309 is defined as $L_x \times L_y \times L_z = 2400m \times 500m \times 300m$. The length increment of the domain
 310 cells is set to 10m in both the longitudinal and transversal directions. The velocity distribution
 311 at the turbine hub (i.e., $Y=0$ m and $Z=90$ m) along the three directions are displayed in Figure
 312 3 along with the spectra produced as a result of the Mann model. The velocities vary throughout
 313 the entirety of the spatial domain, i.e. $U_m \pm 3m/s, V_m \pm 2m/s, W_m \pm 1.5m/s$ for the

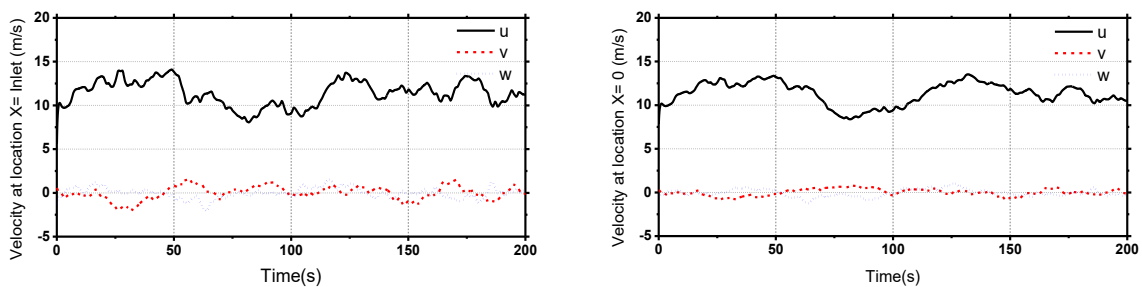


Figure 4 Time history of velocities at turbine hub height ($Z=90$ m) in inlet boundary ($X=-250$ m in Figure 8) and rotor plane positions ($X=0$ m) in CFD calculation without FOWT structure

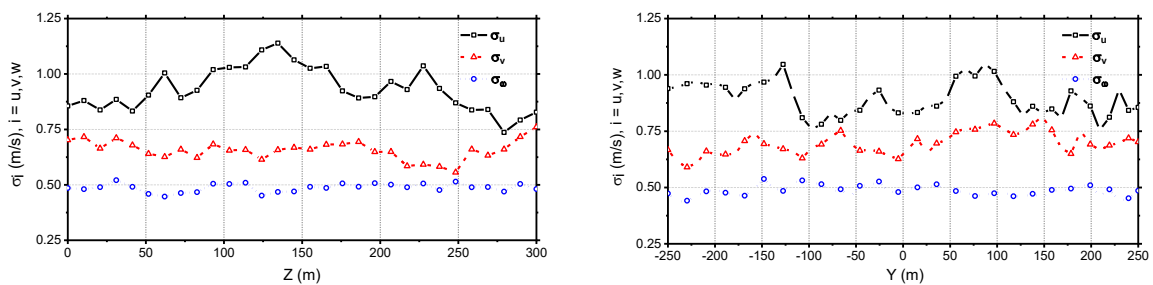


Figure 5 Standard deviation of flow field along the XoY & XoZ plane perpendicular

314 longitudinal and transversal velocity respectively. Figure 3 shows the comparison between the
 315 theoretical transversal velocity one-point velocity spectra against the spectrum obtained from
 316 the Mann model. The values $S_u, S_v,$ and S_w represent the spectrum calculated on the $u, v,$ and
 317 w velocities respectively. Figure 4 presents the velocities at various axial positions in the CFD

318 domain without the FOWT structure where the decay of turbulence could be seen due to the
319 nature of URANS numerical method.

320 Figure 5 shows the standard deviation of the velocity distribution along the XoY and XoZ
321 planes perpendicular to the Z-axis and Y-axis while the turbine rotor locates at Z=90 m and Y
322 =0 m. As we can see from Figure 5, the standard deviation calculated from the Mann model
323 remains consistent with the given one point spectrum. The standard deviation in x, y and z
324 velocity is fluctuated near 1.0 m/s, 0.7 m/s, 0.5 m/s, respectively. These values satisfy the IEC
325 standard [37] of $\sigma_2 \geq 0.7\sigma_1$, $\sigma_3 \geq 0.5\sigma_1$. Despite this, the turbulence intensity (TI) follows IEC
326 standard of TI=0.12 for axial velocity.

327 **3.2 Dynamic motion response and aerodynamic performance of FOWT**

328 The present hydro-aero-mooring CFD solver has been validated through several OC4 Semi-
329 submersible NREL-5 MW FOWT studies which can be seen in our previous papers [25-27].
330 These validations against an 1/50 scaled model operated cover the hydrodynamic responses of
331 the floating structures, the aerodynamic performance of the wind turbine and the tension loads
332 of the mooring lines under both regular wave with a uniform wind field.

333 In the present study, we carried out a validation study with the operating conditions provided
334 in Ref [38]. The uniform inflow speed is 11.23 m/s while the rotor speed is fixed as 7.78 RPM
335 with a collective blade pitch angle of 6.4 degree. The NREL 5 MW wind turbine aerodynamics
336 are investigated without considering the floating platform and the supporting tower.

337 Figure 6 summarizes the time history aerodynamic thrust in 30 s. Three meshes with different
338 densities are generated, which are termed as Coarse (3.8 million), Medium (5.7 million) and

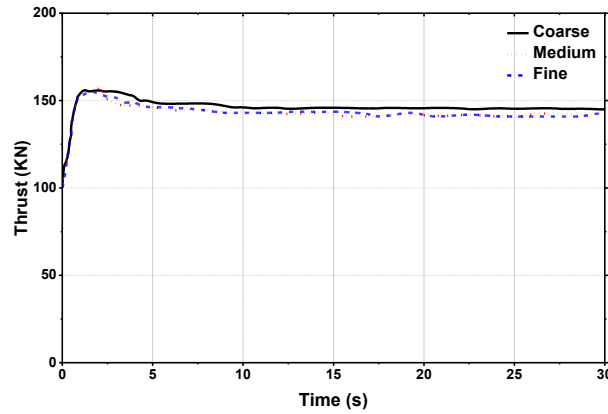


Figure 6 Time history of NREL 5 MW wind turbine thrust force

339 Fine (10.3 million). The time-averaged value is calculated from 20 s to 30 s to eliminate the
 340 initial start-up effects. It can be clearly seen that the difference for thrust between different
 341 mesh is nearly negligible, indicating that the results are independent of the grid. Moreover, the
 342 current predictions are in a good agreement with the experimental data.

Table 1 Mesh sensitivity results of aerodynamic thrust of NREL 5 MW wind turbine

Mesh	Number	CFD	Experimental	FAST
Coarse	3.8 million	143.8 KN	126.1 KN	102.6 KN
Medium	5.7 million	142.0 KN		
Fine	10.3 million	140.8 KN		

343 As the turbulent wind field has been previously validated in section 4.1, thus, we carried out
 344 one more mesh sensitivity study regarding the coupled aero-hydro-mooring FOWT system
 345 considering the floating substructures and the tower under uniform inflow and regular wind
 346 conditions, i.e., LC1.1 (see Table 2 for the operation conditions parameters). This mesh number
 347 refers to 2.7 million, 6.8 million, and 8.6 million for coarse, medium, and fine respectively.
 348 Figure 7 summarizes the time history of the rotor thrust and power predictions under one
 349 sampled rotation period, the aligned results indicate that the results are mesh independent. Thus,
 350 taking the computational cost into consideration, the medium size of the mesh utilized for the
 351 following simulations. To model the present turbulent wind rather

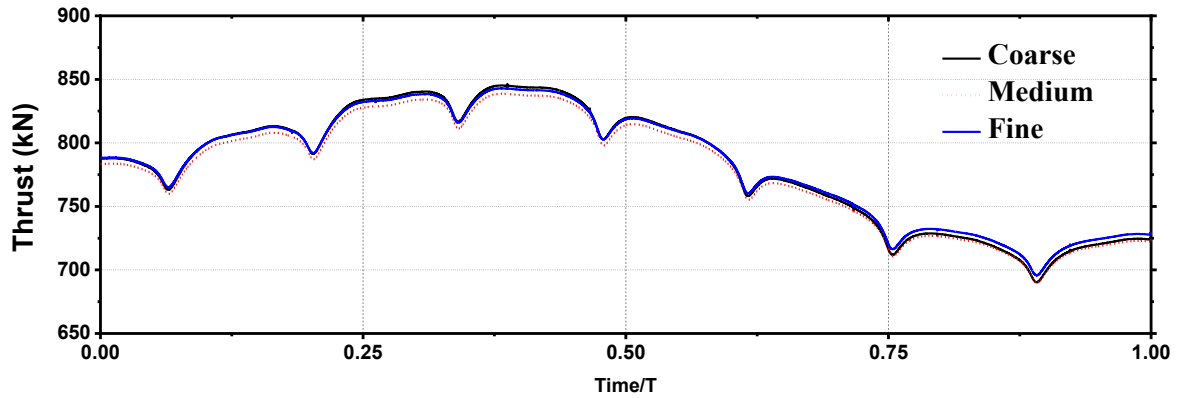


Figure 7 Time history of NREL 5 MW wind turbine thrust under regular waves

352 than constant wind, additional mesh refinement is conducted, and the detail is introduced in
 353 section 4.2.

354 4 Numerical Setup

355 4.1 Case setup

356 The model used in this study is the OC4 semi-submersible NREL 5 MW floating offshore wind
 357 turbine. In regards to the bottom component, the DeepCwind semi-submersible platform is
 358 made up of three offset columns with large heave plate bases, with one centre column used to
 359 support the wind turbine and several connecting braces which act together to stabilize the
 360 floater. The wind turbine subsections include the rotor blades, hub, nacelle, and the tower. The
 361 rotor diameter is 126.0 meters and the hub height is 90 meters above the still water line (SWL).

362

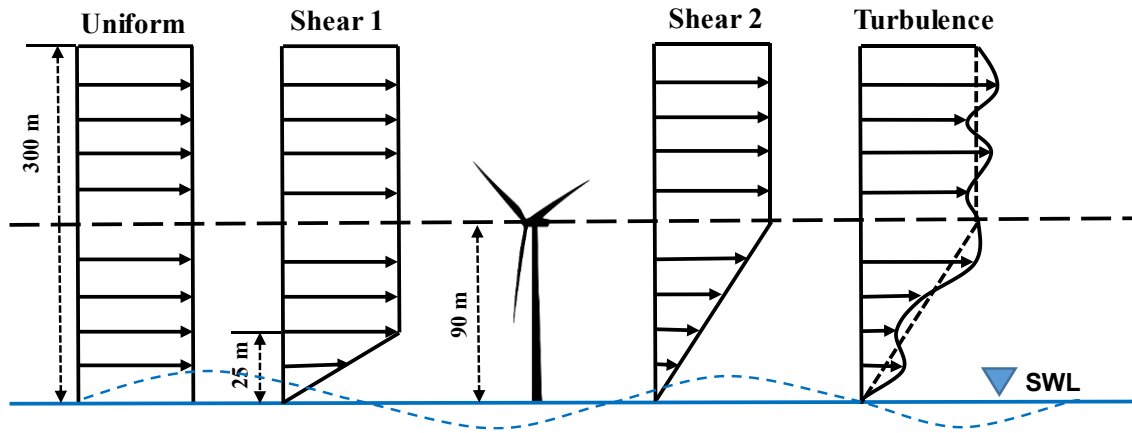


Figure 8 Sketch of four wind fields

Table 2 Physical properties of the selected cases

Wind Fields	Uniform	Shear 1	Shear 2	Turbulence
Load Cases	LC1.1	LC2.1	LC2.2	LC3.1
Waves	Regular wave: $H=7.58\text{m}$, $T=12.1\text{s}$			
Wind: Wind fields				
Characteristics	Time-independent			Time-dependent
Equations	$U_0(x, y, z, t) = \bar{U}_m \left(\frac{z}{H}\right)^n$			
\bar{U}_m (m/s)	$\bar{U}_m = 11.4$			$\bar{U}_m = \bar{U}_m(x, y, z, t) = 11.4$
H (m)	90	25	90	90
n	0	1	1	1

364 In the present study, four different wind fields are examined while the wave condition is kept
 365 constant throughout. A schematic diagram showing these four wind fields is plotted in Figure
 366 6 and listed in Table 2. Three time-independent wind inflow conditions are examined, one
 367 uniform inflow (LC1.1) and two shear wind inflows (LC2.1 and LC2.2). The turbulent wind,
 368 illustrated in Figure 8 is time-dependent as LC3.1. For the time-independent shear wind, the
 369 shear layer is picked up as 25 meters in LC2.1, and 90 meters in LC2.2. The 25 meters height
 370 is a height which can be found in other investigations [14], however, 90 meters is selected for
 371 two reasons. Firstly, in the LC2.1, $H=25\text{meters}$ is too short to fully cover the region where the

372 turbine blades rotate, thus, we anticipate that the influence of such shear flow on the
373 aerodynamic characteristics of the wind turbine is minimal. The LC2.2 with H=90 meters is
374 expected to yield significantly different results from LC2.1. In addition, to study the turbulence
375 incoming wind, the Mann turbulence box generates a shear layer between H=0 (SWL) to the
376 turbine rotor centre at H=90 meters. Therefore, LC2.2 is set up in this study. The time-mean
377 velocity U_m is 11.4m/s. The wave condition for all four cases is Stokes second-order regular
378 wave as wave height and wave period refers to 7.58 meters and 12.1 seconds, the commonly
379 used sea state in North Sea [38]. The blade pitch angle is maintained as a constant of 0° and
380 the rotor speed is fixed to 12.1 RPM under rated wind speed suggested by NREL [39]. The
381 turbine blades are regarded as rigid, and thus no aero-elasticity of blade is taken into account
382 and also no blade pitch and generator torque controller are used in the present model.

383 4.3 Computational domain and boundary conditions

384 *Table 3 Main parameters of the CFD computational domain and Mann turbulence box, d refers to the spacing*
385 *of offset columns of platform (50 m)*

	OpenFOAM (CFD)	Mann Turbulence Box
Domain Size	$750m \times 400m \times 500m$ $15D \times 8D \times 10D$	$2400m \times 500m \times 300m$ $48D \times 10D \times 6D$
Domain Grid	6844520 cells	$240 \times 50 \times 30$ cells
Grids around WT	3549010 cells	N/A

386 As was previously mentioned, the dimensions of the CFD domain are different from those of
387 the Mann turbulence box as we can see in Table 3. As shown, the X and Y dimensions of the
388 Mann turbulence box are larger than those of the CFD as suggested in [12, 15, 40]. This allows
389 us to achieve the spatial interpolation of the turbulent velocity field originally generated in the
390 Mann box. However, the Z dimension of the Mann turbulence box is smaller than that of CFD
391 domain. This is due to the inclusion of the water wave phase in CFD modelling, e.g. a water
392 depth of 200 m is included.

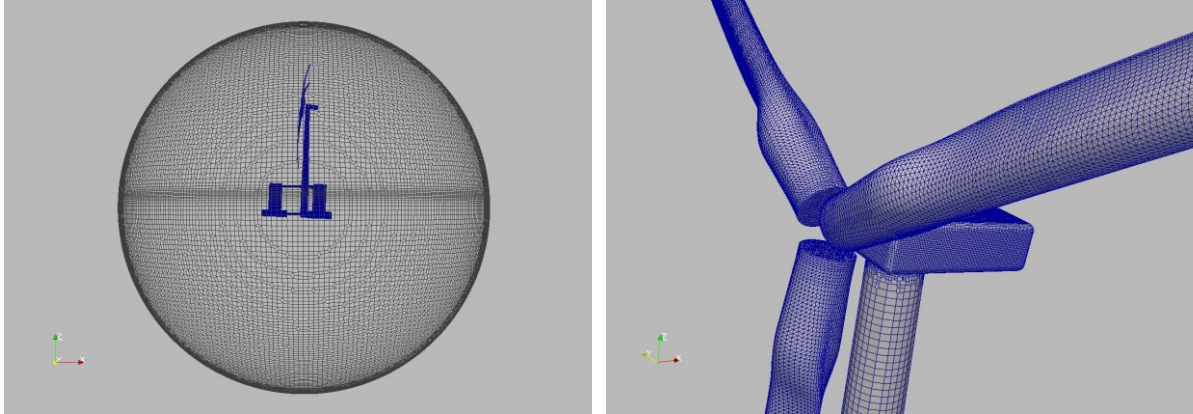


Figure 9 Computational mesh of NREL 5 MW semi-submersible FOWT

393 A built-in arbitrary mesh interface (AMI) method in OpenFOAM can be used to analyse the
 394 motion of an OC4 semi-submersible NREL 5 MW FOWT. Figure 9 shows the partial mesh on
 395 the structure and AMI surface of the entire computational domain. A built-in tool
 396 (snappyHexMesh) has been adopted to generate the computational mesh. The total mesh for
 397 the present CFD computation for all four simulations equates to 6844520. Grid refinement is

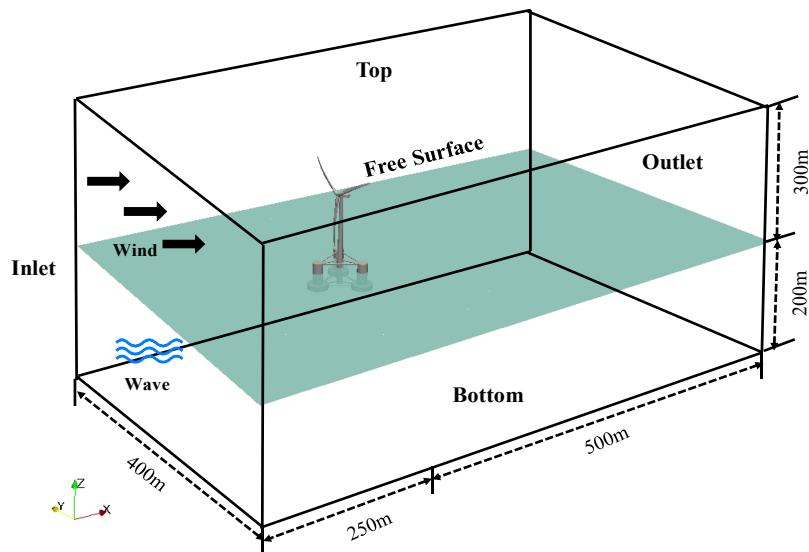


Figure 10 Sketch of CFD computational domain of FOWT modelling

398 applied near the free surface where the wind turbine blades and the turbine wake can be found.
 399 Eight layers of boundary layer mesh with the first layer grid thickness of 0.4mm and a
 400 progression rate of 1.1 is added. This is to ensure the y^+ value is in the range of [30,300] while
 401 a wall function is adopted for near wall treatments. In addition, relaxation zones are set to

402 achieve a better wave quality and to reduce the wave reflection. The length of these zones are
403 defined as follows, i.e., inlet relaxation zones: one wave length, and the outlet relaxation zones:
404 two wave lengths. The origin of the coordinate system is located at the FOWT platform centre
405 and the flow direction is along the positive x -axis.

406 The sketch of the boundary conditions of CFD domain is shown in Figure 10. At the inlet
407 boundary (where $x = -250m$), the velocity is defined as the prescribed incident regular wave
408 together with up turbulent, uniform and shear winds. The κ and ω , is estimated by using
409 Equations (18 and 19) referred by Tian's study [41], where I is the turbulence intensity and $\frac{\mu_t}{\mu}$
410 represents the viscosity ratio.

$$\kappa = 1.5(UI)^2 \quad (18)$$

$$\omega = \frac{\rho\kappa\mu_t^{-1}}{\mu\mu} \quad (19)$$

411 The gradient of velocity, κ and ω is set to zero at the outlet boundary ($x = 500m$). The front
412 and back boundaries ($y = \pm 200m$) are imposed symmetrically and the top and bottom
413 boundaries ($z = 300m$ and $-200m$) are set as the zero gradient. The non-slip wall boundary
414 with zero pressure gradient is defined on the patches of the FOWT.

415 The time step is set as small as 0.001s, i.e., 1/4950 of T_{rot} for one turbine rotation, 1/12100 of
416 one wave period. For LC1.1, LC2.1, LC2.2 and LC3.1, it takes nearly 580 hours using High
417 Performance Computing facility with 200 cores running in parallel for 200 seconds, i.e., the
418 time span covers around 40 rotations for a wind turbine or 17 incident wave periods.

419 5 Results

420 5.1 Wind turbine aerodynamic characteristics

421 Figure 11 shows the time history of the rotor thrust and power predictions under two sampled
422 wave periods (132s-156s) when they are exposed to uniform, shear and turbulent flow
423 conditions. Then, by utilising both NREL FAST V8 and TurbSimV1.06 [8] [42], we are able
424 to compare these results against the BEM results achieved previously. We know that the
425 instantaneous time is non-dimensionalized by the incident wave period (T), whilst an estimate
426 of the thrust force of CFD can be calculated by using the sum of the aerodynamic force exerted
427 on all three blades along the x direction. Consequently, the power can also be calculated by
428 multiplying the rotor torque against the angular velocity of the rotor blades. Non-dimensionally,
429 the formula: $C_T = Thrust / 0.5\rho R U^2$ can be used to work out the thrust coefficient. Similarly,

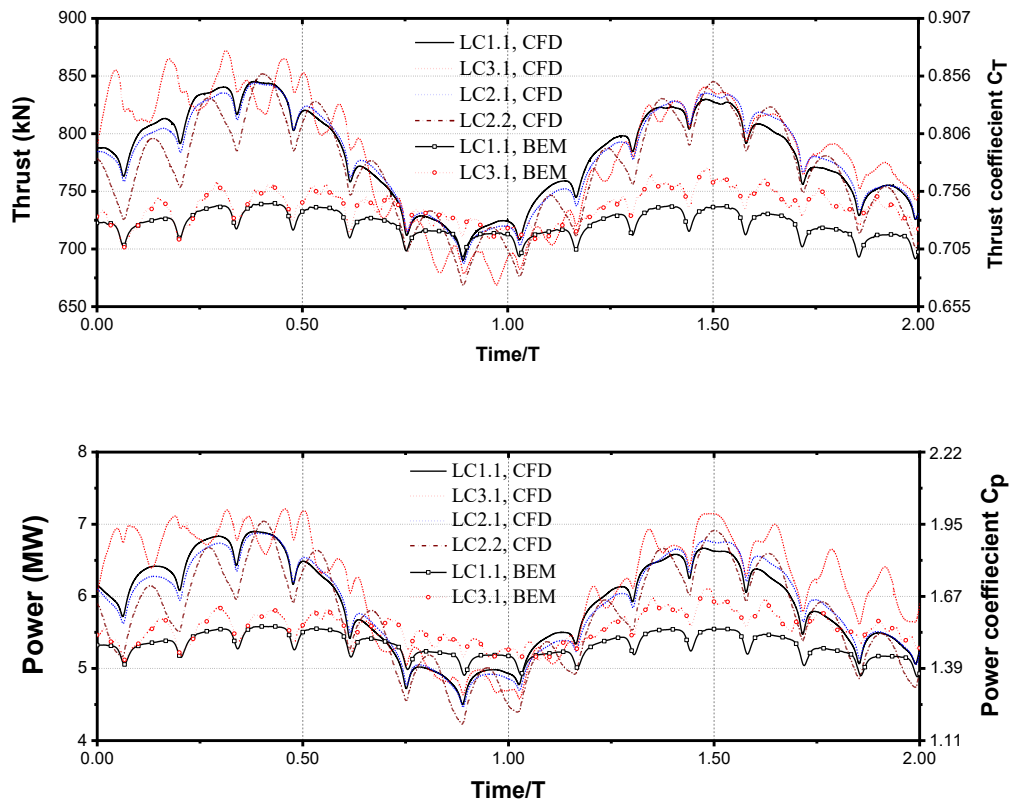


Figure 11 Thrust and power outputs of FOWT under uniform, shear and turbulent flow

430 the power coefficient can be estimated by applying the formula $C_p = Power/0.5\rho RU^3$, in
 431 which, R represents the rotor radius and U stands for the wind speed.

Table 4 Statistics of thrust and power of wind turbine under different wind fields

		CFD				NREL FAST	
		Uniform wind (LC1.1)	Shear wind (LC2.1)	Shear wind (LC2.2)	Turbulent wind (LC3.1)	Uniform wind (LC1.1)	Turbulent wind (LC3.1)
Thrust (KN)	Max/Diff	846.4 (0.00%)	845.1 (-0.15%)	851.8 (0.65%)	872.2 (3.05%)	739.8 (0.00%)	770.4 (4.13%)
	Min/Diff	690.3 (0.00%)	687.4 (-0.43%)	668.3 (-3.19%)	668.6 (-3.14%)	693.2 (0.00%)	701.1 (1.14%)
	Mean/Diff	781.3 (0.00%)	781.3 (0.00%)	771.7 (-1.22%)	783.7 (0.31%)	723.2 (0.00%)	735.1 (1.65%)
	σ	39.7	40.5	43.8	53.1	10.2	14.3
Power(MW)	Max/Diff	6.90 (0.00%)	6.87 (-0.43%)	7.04 (2.02%)	7.21 (4.49%)	5.58 (0.00%)	6.11 (9.49%)
	Min/Diff	4.50 (0.00%)	4.46 (-0.80%)	4.22 (-6.02%)	4.58 (1.70%)	4.90 (0.00%)	5.10 (4.08%)
	Mean/Diff	5.88 (0.00%)	5.89 (0.17%)	5.75 (-2.21%)	6.16 (4.76%)	5.34 (0.00%)	5.54 (3.74%)
	σ	0.63	0.64	0.67	0.76	0.15	0.21

432 Referring to Figure 11 again, we can see that the values for both CFD and NREL FAST display
 433 a similar pattern in regards to the rotor thrust force and the overall power output of the wind
 434 turbine. Under uniform inflow conditions (LC1.1), the thrust and power outputs show a similar
 435 pattern, i.e., the numerical predicted peak values are smaller than those obtained from FAST.
 436 This might be due to the fact that the floater motion on the turbine wake flow is taken into
 437 consideration via solving the URANS equations directly, while the BEM based tool (NREL
 438 FAST) adopts an empirical correction dynamic wake model . Similar findings are noted in
 439 References [12, 43, 44] where the variance of the peak thrust/torque is nearly $\pm 8\%$. In the
 440 present simulation, the difference goes to nearly 11%. At certain time instances, (0.06T, 0.20T,
 441 0.33T, 0.47T, etc.), we are able to see a few local minimum values appear along both thrust
 442 force and power curve simultaneously. From the data, we can see that these sudden dips vary
 443 between 5-7% of the mean thrust force and power. These can be observed at every 1/3 rotation
 444 of the wind turbine, where the blades rotation aligns themselves front of the tower.

445 The results obtained by comparing different wind fields suggests that in the presence of wind
 446 turbulence, both the peak of the thrust and power is increased when compared against a time-

447 independent uniform/shear wind. In addition to this, CFD is able to predict a larger magnitude
 448 of fluctuation than the FAST results. Aside from this, however, it is also observed that there is
 449 a relatively low frequency variation in the thrust and power, which could potentially be directly
 450 caused by the turbulent decay which is associated with the URANS CFD modelling used in
 451 this study.

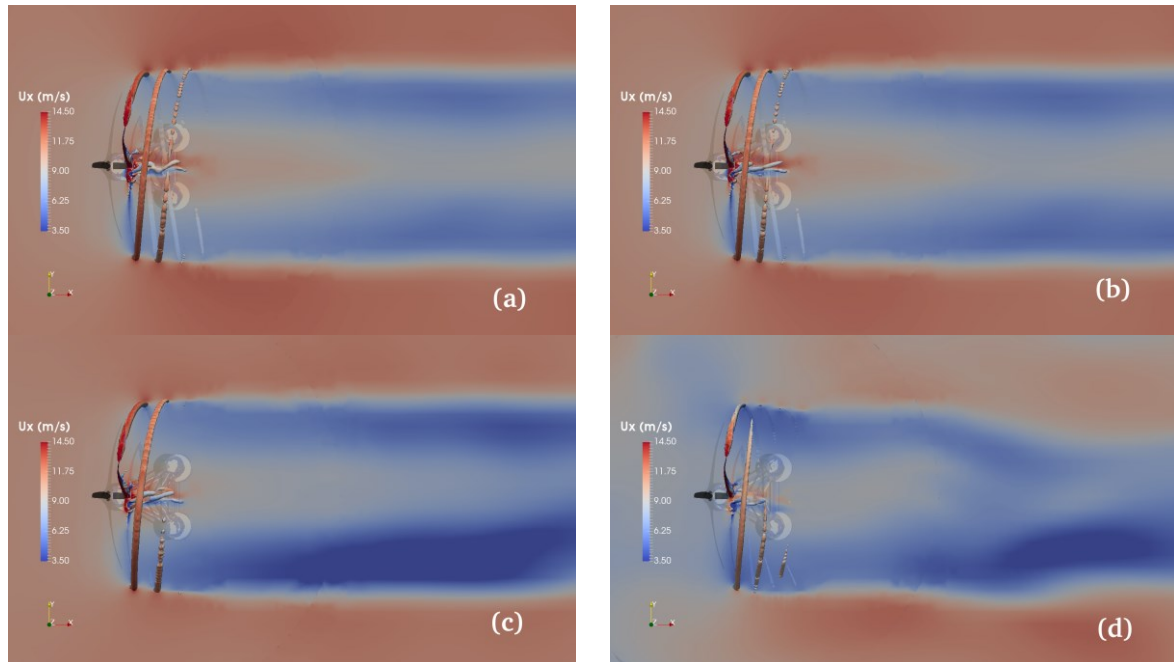


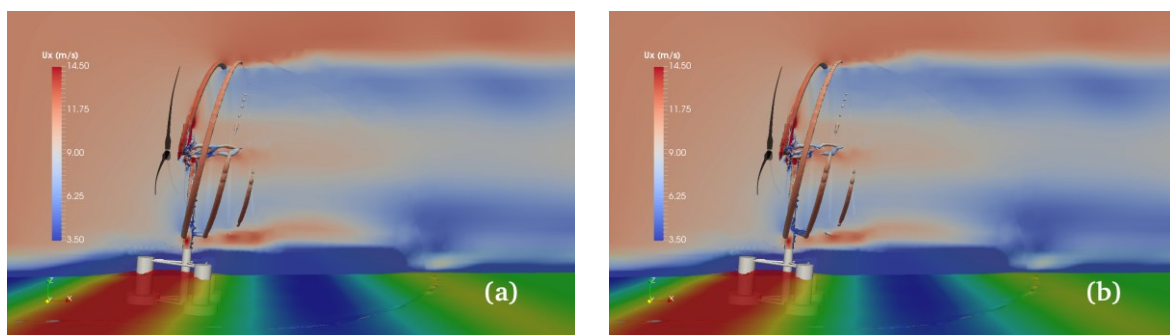
Figure 12 Instantaneous flow field in a horizontal sectional plane coloured by axial velocity located at the hub height ($z=90$ m) at instant time of $0.9T$. (a): LC1.1, (b): LC2.1, (c): LC2.2, (d): LC3.1

452 To allow us to develop a better understanding of the consequence that turbulent wind has on
 453 the aerodynamic performance of a wind turbine, we must carry out a statistical analysis of the
 454 data. The results of this analysis can be seen, summarized above in Table 4 for the peak
 455 and time-mean parameters. We can see that the Time-mean thrust results obtained by using
 456 CFD indicate that despite the mean magnitude being nearly identical for the uniform, shear
 457 wind and turbulent wind, (e.g. 783.7KN, 781.3KN, 771.73KN, 781.3KN for LC1.2, 2.1, 2.2
 458 and 3.1 respectively), the standard deviation values for turbulent wind (LC3.1) is seen to be
 459 reasonably larger than the values obtained for the time-independent wind field, i.e., 39.7KN,
 460 40.5KN and 43.8KN for LC.1.1, 2.1 and 2.2, respectively. This observation can also be found

461 in the results of the NREL FAST analysis. On top of this, the difference between the peak thrust
462 and power between uniform and turbulent wind is also slightly larger than their respective time-
463 mean values. However, it should be taken into account that the thrust and power are both largely
464 controlled by the wind speed that locates at the upstream region of the rotor blades. Because of
465 this, the large time-variable peak thrust which was found in the presence of turbulence does
466 not necessarily suggest that the time-mean thrust is larger in the absence of turbulence.

467 5.2 Wind turbine wake profile

468 Figure 12 below shows the instantaneous velocity contour on a horizontal XoY plane at Z=90
469 m where we can see the effects of either the presence or absence of turbulence at a time instant
470 $t=0.9T$. The initial FOWT positions are coloured in black which proves that that the floating
471 structures are interacted with the turbine wake. At these specific values, we can see exactly
472 where the rotor thrust output reach a trough in Figure 11. The vorticity plots rendered as the
473 ISO surfaces of Q is set to 1. This is coloured by the axial velocity [45]. Using the data and
474 comparing all four figures, a typical spatial variation can be clearly seen and alongside this,
475 there are some clear-cut differences between uniform/shear wind conditions and turbulent wind
476 conditions. In the presence of turbulence, we can see that, the wind field upstream of the wind
477 turbine clearly shows a lower speed regime



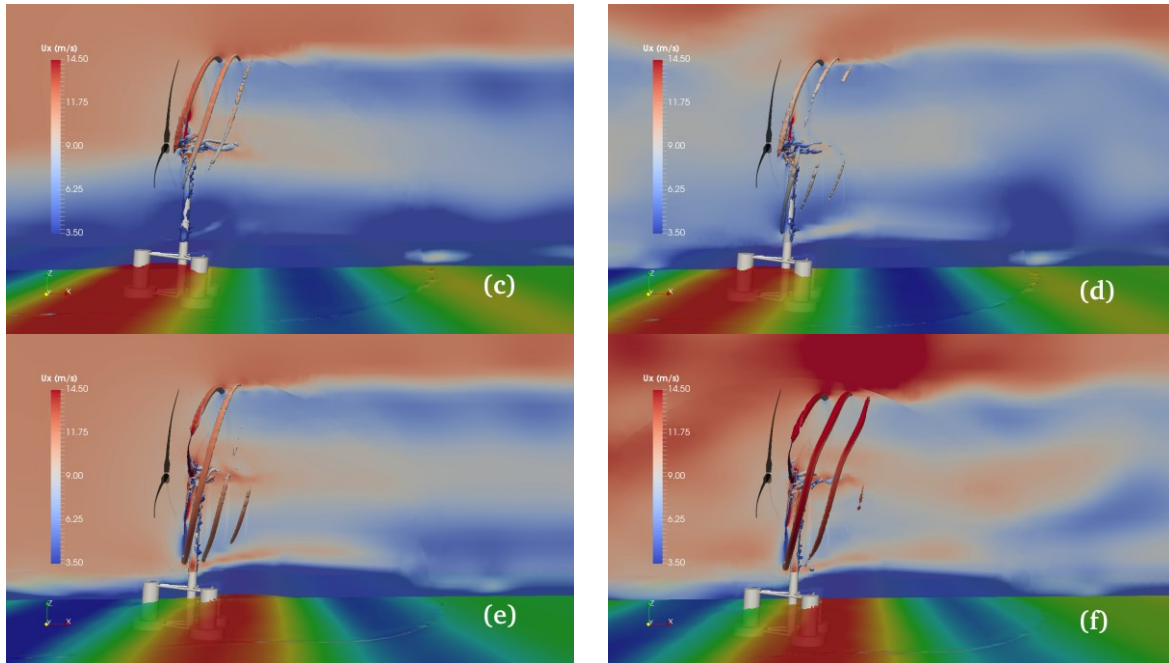


Figure 13 Instantaneous flow field in a sectional vertical mid-plane (XoZ) coloured by axial velocity: (a) LC1.1 (b) LC2.1 (c) LC2.2 (d) LC3.1 at time $t=0.9T$; (e) LC1.1 (f) LC3.1 at time $t=1.4T$

478 compared to conditions when turbulence is absent. Referring to Figure 11, where the thrust
 479 time sequence is plotted, at the point where $t=0.9T$, the instantaneous thrust value when
 480 turbulence is present is less than the instantaneous thrust value calculated when turbulence is
 481 absent. This smaller value in the instantaneous thrust can be attributed to the low speed regime
 482 upstream of the wind turbine. This effect can also explain why the wake downstream of the
 483 turbine looks to be more unsteady and non-uniform. As a result of this, the turbulent diffusive
 484 nature is observed to extend further down into the weaker vortices forming between the hub
 485 and the blades.

486 Figure 13 shows the vertical sectional view with respect to the flow field at the mid-plane (XoZ)
 487 of the computational domain. We can see that both in the absence and presence of turbulence,
 488 at two specific time instances, (i.e., $t=0.9T$ and $t=1.4T$) the minimum and maximum thrust is
 489 generated, while also factoring in the free surface of water-air. From Figure 13, we can see the
 490 airflow close to the air-wave free surface is significantly more affected by the water wave
 491 propagation compared to the airflow which is further away. This represents the wind-wave

492 interaction which is coupled in the CFD modelling. This observable effect can be attributed to
493 the decreased air velocity which can be seen above both the wave crests and troughs near the
494 free surface. It should not go unmentioned the airflow field found around the wind turbine is
495 not significantly affected. Similar to the findings from Figure 12, we can see that the turbine
496 wake at the XoZ plane (which is represented by the velocity field) becomes increasingly non-
497 uniform when turbulence is present compared to the conditions when turbulence is absent.
498 Figure 14 shows the axial velocity distribution when a non-dimensional form is present
499 U/U_∞ in the wake region ranging from $x=0.5D_{\text{tr}}$ to $3.0D_{\text{tr}}$ downstream. Using Figure 14, we
500 are able to see the velocity found at the rotor, (i.e., $y/D_{\text{tr}}=0$), decreases apparently from the
501 near-wake to the far wake, whilst the velocity found at both the top and bottom blade tips, i.e.,
502 $y=\pm 0.5D_{\text{tr}}$ are found to trend closer to the rated wind speed. In addition, we can see that when
503 compared against the time-independent wind fields (LC1.1, LC2.1 and LC2.2), the presence of
504 wind turbulence (LC3.1) results in quick diffusion of the wake. This is demonstrated by a rapid
505 change of axial velocities between $-0.5D_{\text{tr}} < Y < 0.5D_{\text{tr}}$. These findings are supportive to the
506 studies by Li et al. [12] for an onshore fixed wind turbine, e.g. the floating concepts have
507 negligible impacts on the turbine wake velocity distribution along the horizontal sectional plane
508 at hub height when they are compared with onshore turbines.

509 Figure 15 plots the instantaneous turbulence intensity (TI) contour at the $Y=0$ m plane. Since
510 the results gathered from LC1.1, LC2.1 and LC2.2 are almost identical to each other, the only
511 comparison that can be made is between conditions with uniform wind (LC1.1) and conditions
512 with turbulent wind. We can see that the plots above in Figure 15 show a large

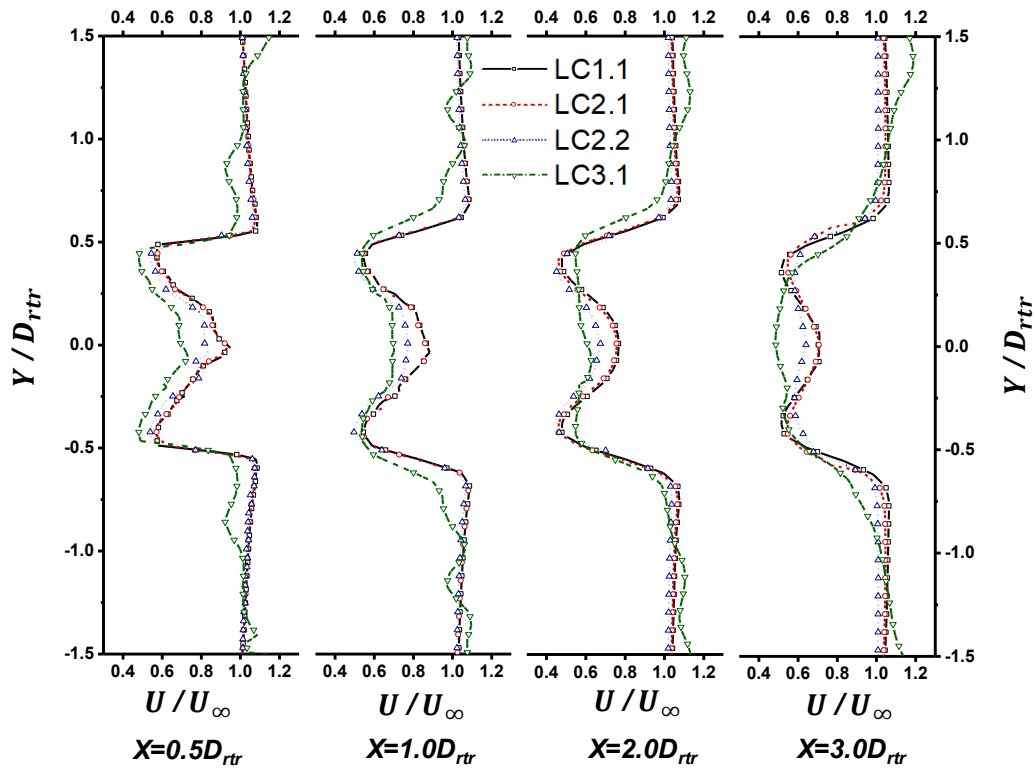


Figure 14 Axial velocity at different axial positions at hub height ($Z=90$ m) in the wake region at $t=0.9T$

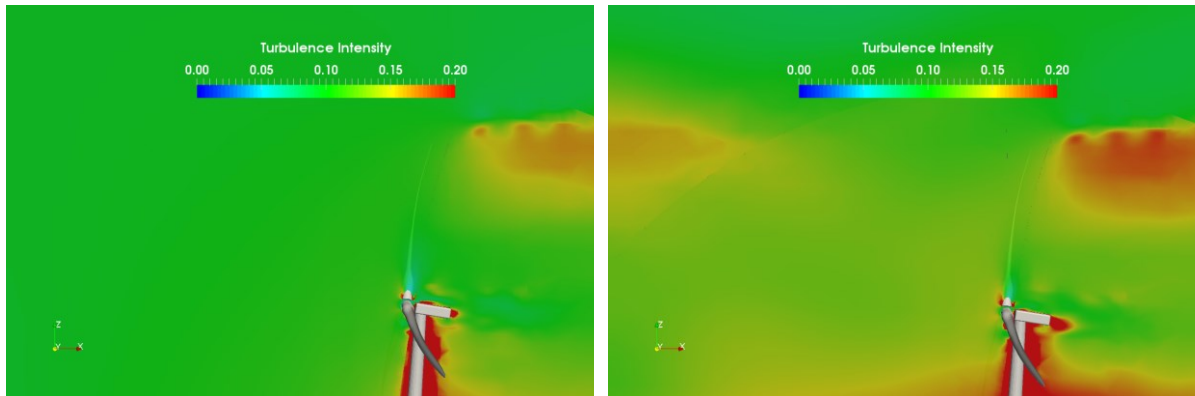


Figure 15 Turbulence intensity distribution along the XoZ plane at instant time of $0.9T$.
Left: LC1.1, right: LC3.1

513 variation in the TI regime. This variation is not unique to only the rotor as it can also be found
 514 at the tip of the blade. More detailed information regarding the variation can be seen in Figure
 515 16, where the turbulence intensity profiles are recorded at the hub height. We can see here that,
 516 similar to the velocity profile shown in Figure 14, the TI also dissipates faster for LC3.1. It
 517 should be noted however, that at the blade tip of $y=\pm 0.5D_{rtr}$, the TI value is found to be greater

518 in the presence of turbulence than in the absence of turbulence.

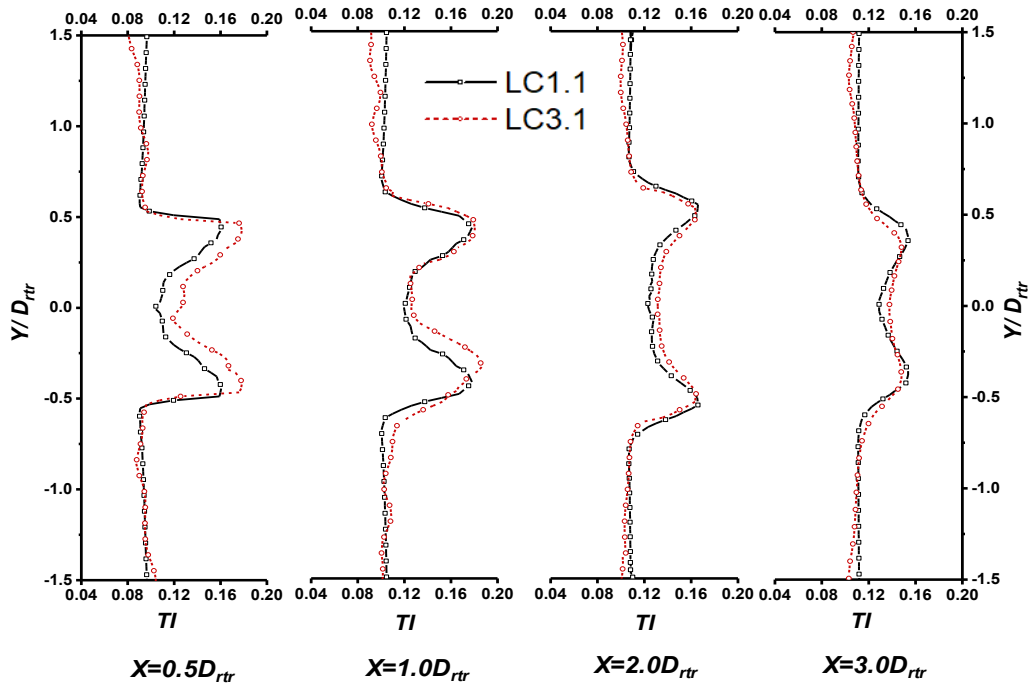


Figure 16 Turbulence intensity at different axial positions at hub height ($Z=90\text{ m}$) in the wake region at $t=0.9T$

519 Figure 17 shows the contours of the airflow field at four different span-wise sections of blade-
 520 1, i.e., the blade of the turbine with an azimuth angle of 0 degrees. This is coloured by the axial
 521 velocity. Figure 18 shows the pressure distribution along the surface of foils, represented by
 522 C_p alongside the schematic diagram which indicates the slices along the blade span direction.
 523 This is represented by r/R . Factoring in the aspect that no aero-elastic feature of the blade is
 524 taken into account for the conducted simulation, the Angle of Attack (AoA) of the varying
 525 slices of the blade is constant. These values are provided in the NREL report [39]. As shown
 526 in Figure 17 (a), the flow separation occurs between 1/3 to 1/2 chord lengths from the foil
 527 leading edge under all conditions and at varying r/R levels.

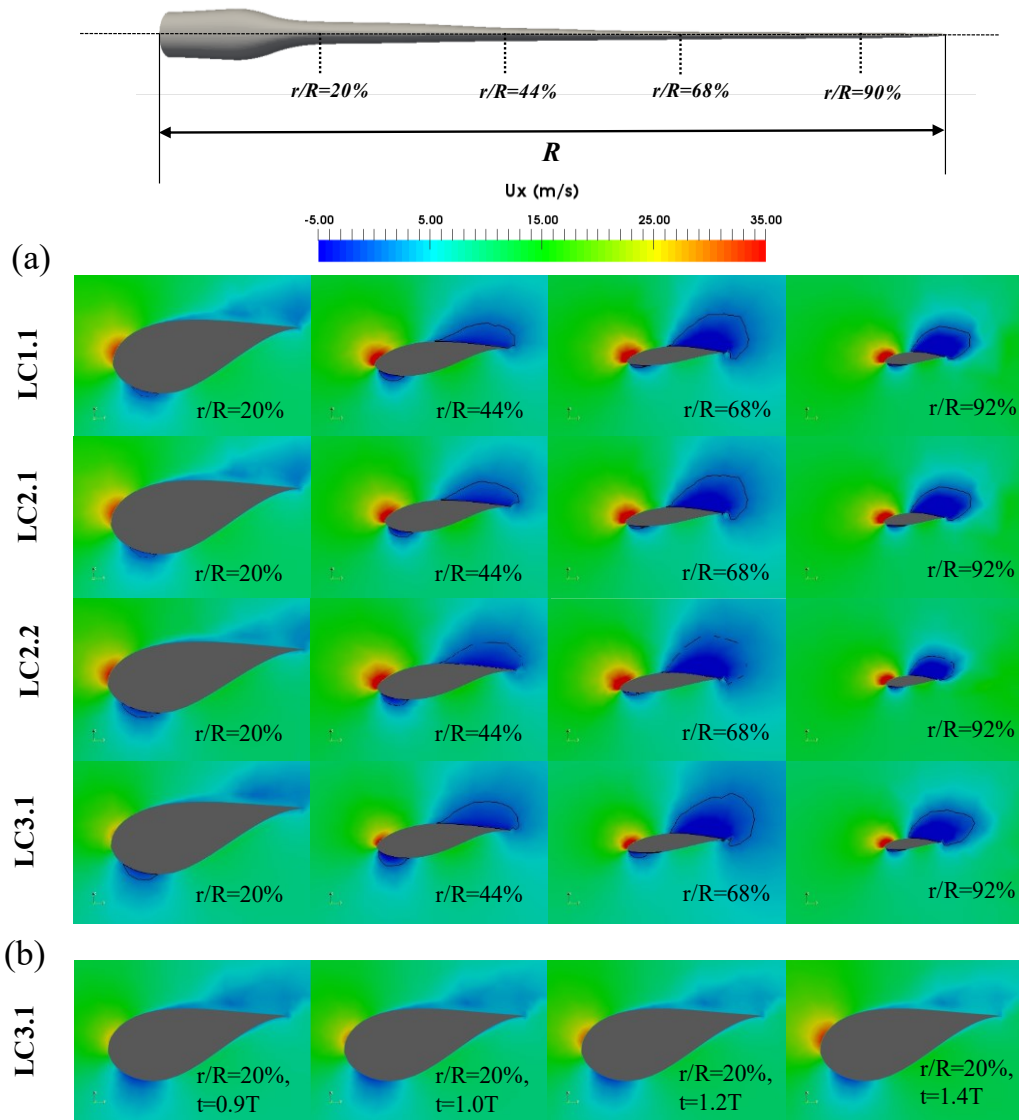


Figure 17 Instantaneous flow field of (a) axial velocity along different blade sectional views at time $t=0.9T$
 (b) axial velocity along blade sectional views at $r/R=20\%$ at different time instants for LC3.1

528 This phenomenon can be seen to start along the top surface of the foil, before continuing and
 529 extending to the trailing edge. We can see that both the recirculation regime (which is
 530 associated with a reversed pressure gradient) and the negative velocity regime become more
 531 profound as the flow moves from the foil root to the foil tip, with an increasing value of r/R . In
 532 addition, to illustrate the unsteady feature, Figure 17 (b) plots the axial velocities at $r/R=20\%$
 533 for LC3.1 at different time instants between $t=0.9T$ and $t=1.4T$, where the thrust increases
 534 gradually (see Figure 11). As we can see from this figure, with the increase of incoming flow

535 velocity, the flow separation near the trailing edge becomes weaker and weaker, leading to the
 536 increase of lift force and thus the overall thrust.

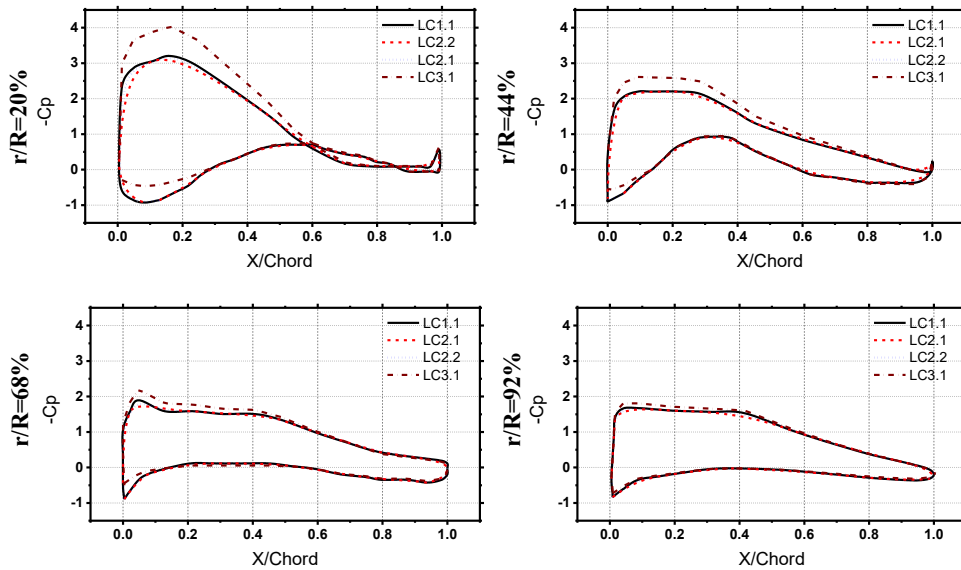


Figure 18 Pressure distribution at different axial positions at instant time $t=0.9T$

537 We can see that by comparing the pressure distribution shown in Figure 18, that when the value
 538 of r/R is equal to 20%, LC3.1 is found to be significantly different than the other cases. This is
 539 especially noticeable at the regime $x/Chord < 0.5$, suggesting that turbulence wind has a
 540 significant influence on the foil surface pressure distribution, which ultimately results in a
 541 change in the lift force and thrust/power. However, as the r/R value increases towards a value
 542 of 0.98 (where the blade slice ends up in its tip position), this discrepancy becomes less and less
 543 apparent. This finding then suggests that varying levels of turbulence will impact decays from
 544 the blade root to the blade tip. This conclusion is consistent with the turbulent boundary layer
 545 development around the slender shape of the blades and the turbine tower itself.

546 5.3 Shear wind layer thickness

547 We can see from the above results that there are a few distinct differences between the results
 548 gathered from uniform wind LC1.1, shear wind LC2.1 and LC2.2. If we consider the idea that
 549 a uniform wind can be treated as the shear layer height of zero, then we must conduct a further

550 study to provide us with enough information to form a detailed explanation regarding to the
 551 impact of shear wind layer thickness to the FOWT aerodynamic.

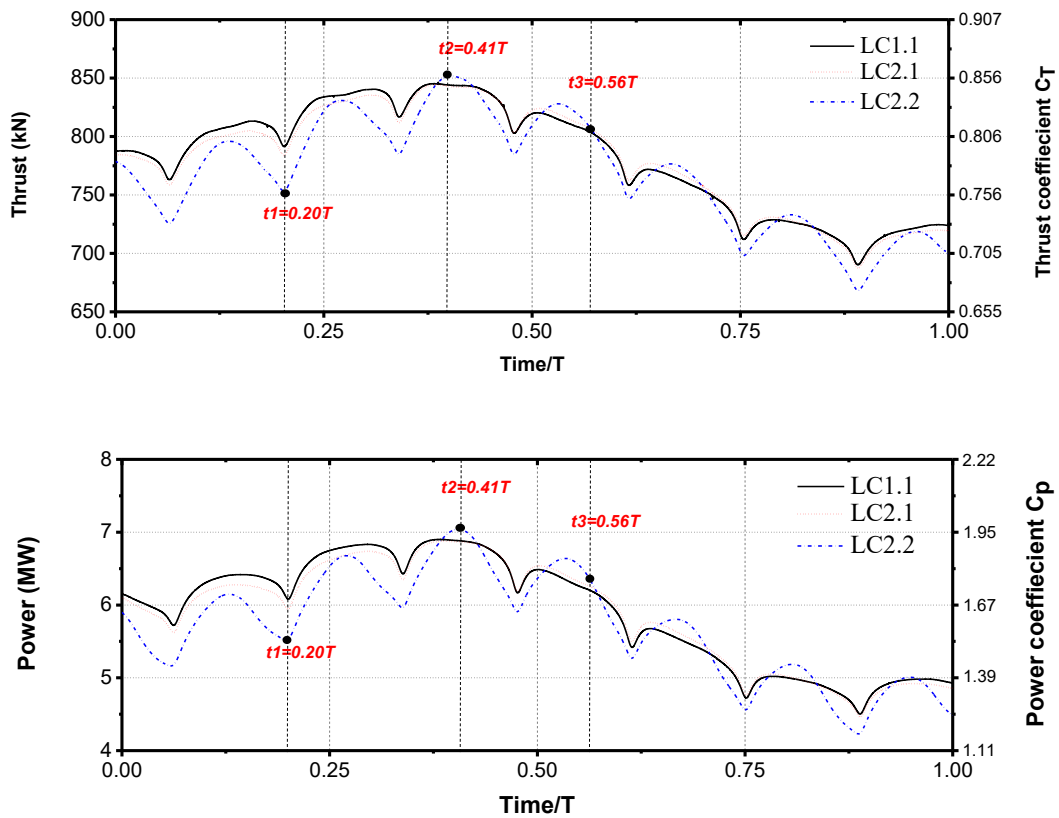


Figure 19 Thrust and power outputs of FOWT under time independent wind fields

552 Figure 19 plots a zoom-in curve using the rotor thrust/power data shown previously in Figure
 553 11. There are three specific times selected for the purpose of plotting: $t_1=0.20T$, $t_2=0.41T$ and
 554 $t_3=0.58T$. These three times are selected as they correspond to the specific times at which a
 555 local minimum, maximum and moderate thrust/power appears, respectively.

556 From Figure 19, we can see that regular local troughs and crests develop in the time sequence
 557 thrust/power curve regardless of the height of the wind shear layer. The local minima at $t=0.20T$,
 558 $0.34T$, $0.48T$, etc. appear in the same time instances as when the blades pass in front of the
 559 tower. This phenomena can also be found in various previous studies [19] [20] [27], and it has
 560 been named as the tower shadow effect. When we compare between the three different shear
 561 conditions, we can see that in all instances, LC2.2 always has a smaller thrust in comparison to
 562 the others. Since we know that the shear height of LC2.2 is 90 meters, we can draw the

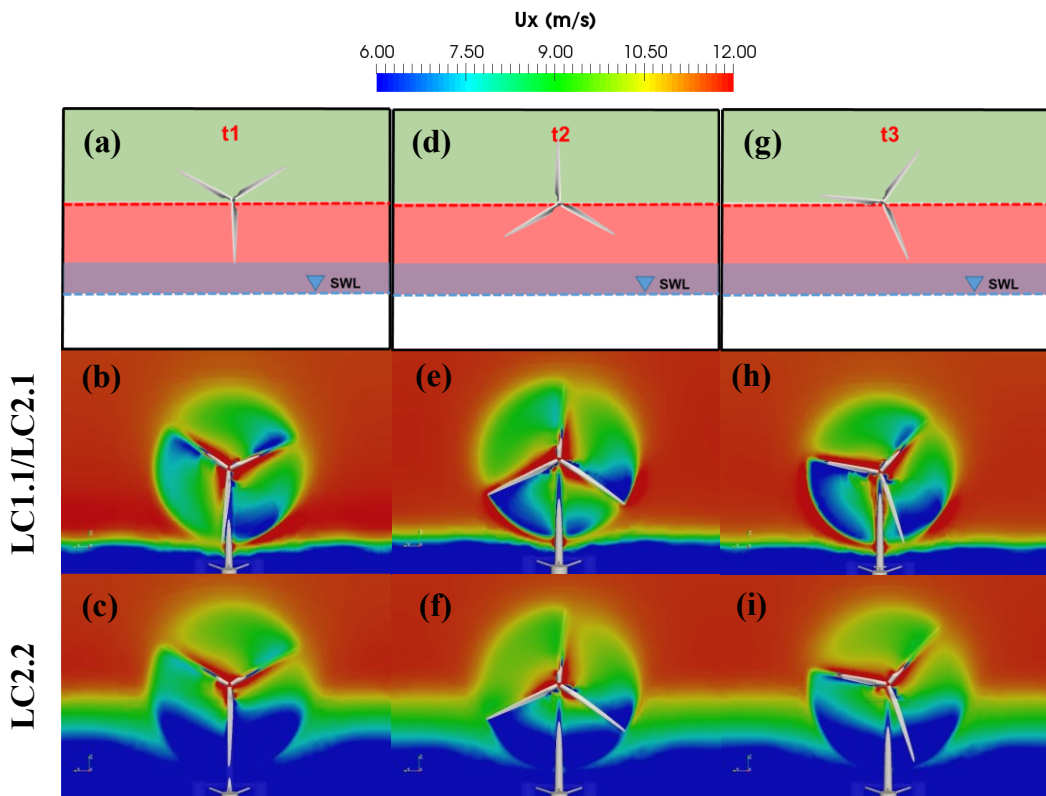


Figure 20 The sketch of the turbine blade position and the instantaneous flow field at a vertical sectional plane (YoZ) at three time instances

563 conclusion that the shear thickness at this level has a significant impact on the aerodynamic
 564 characteristics of the wind turbine. This effect becomes most prominent at a time instance of
 565 $t_1=0.20T$, where the thrust can be seen to decrease 6% from LC1.1 to LC2.2. The reasoning to
 566 explain this phenomenon can be found in the blade position and velocity contours displayed in
 567 Figure 20. If we take the points $t_1=0.20T$ in Figure 20 (a) to (c), we can see that in the low
 568 velocity zone (indicated by a large area coloured blue in Figure 20 (c)) for LC2.2, this extends

569 away from the platform towards the centre of the rotor. This low-speed regime is found to
570 mainly occupy the area closest to wave-air free-surface for LC2.1 shown in Figure 20 (b). As
571 a result of this low speed regime, smaller wind turbine blades may generate lift force and thus
572 resulting in a smaller torque and thrust.

573 One interesting thing to note is that as shown above, the shear layer impact is not always
574 constant at any given time instance within a single wave cycle. We can see from Figure 20, at
575 specific time instances of $t=0.34T$, $0.48T$, $0.62T$, $0.76T$ and $0.90T$, the shadow effect can also
576 be spotted, similar to the occurrence at the point where $t_1=0.20T$. In these instances however,
577 it can be seen that the discrepancy among LC1.1, LC2.1 and LC2.2 is not as significant as
578 $t_1=0.20T$. Therefore, we can conclude that, at the mentioned time instances, the motion of the
579 floater leads to the blade inclination to the incoming wind and also a reduced swept area of the
580 turbine can be seen, resulting in the smaller thrust/power predictions.

581 Now, taking the point where $t_2=0.41T$, the local peak thrust/power is achieved when the
582 azimuth angle of the three blades are $0^\circ, 120^\circ, 240^\circ$, respectively. We can see that at this one
583 moment, the disparity between LC1.1, LC2.1 and LC2.2 is extremely minimal. Compared with
584 LC1.1 & 2.1, the low velocity can be seen to occupy a slightly smaller area as displayed in
585 Figure 20 (e) & (f). Because of the decrease in the area which is occupies, it now has less of an
586 impact on the thrust/power. This effect can be clearly seen at the point $t_3=0.58T$ in Figure 20
587 (g) to (i), where the wind turbine is experiencing a moderate thrust/power, compared to the
588 greater values which it was previously experiencing.

589

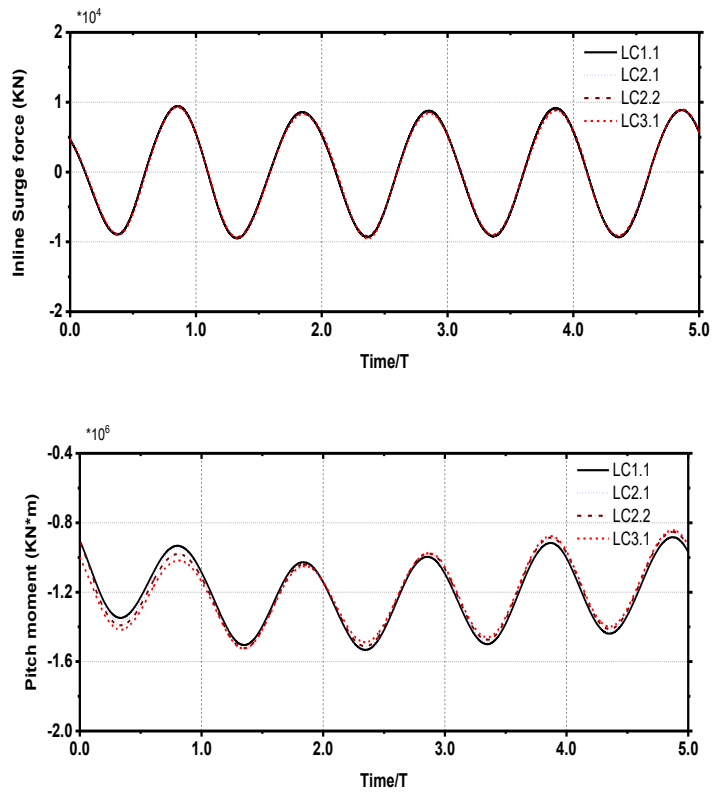


Figure 21 Inline surge force and pitch moment of the FOWT under different wind fields

590 **5.4 Hydrodynamic response**

591 Not taking into account the previously mentioned details regarding the aerodynamic of a wind
 592 turbine, the involvement of turbulent wind could also be influencing the FOWT hydrodynamic

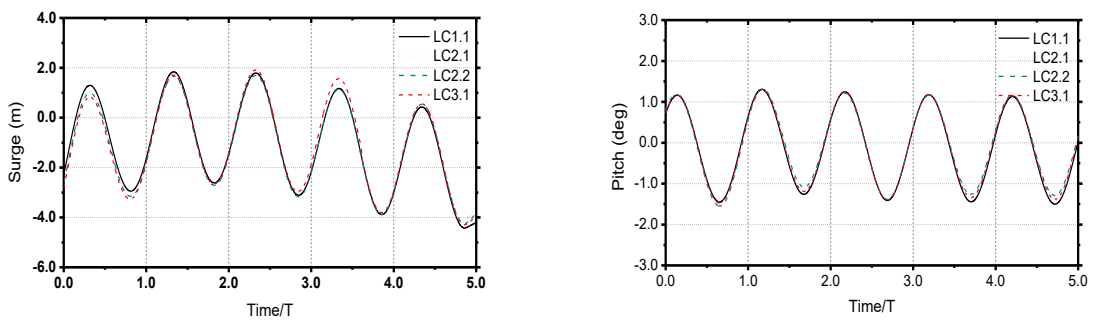


Figure 22 Surge and pitch motion under different wind fields

593 responses. Figure 21 plots the inline surge force and the pitch moment relative to the tower root
 594 of the full FOWT under five sampled regular wave periods (132s-192s). From these results, we

595 can conclude that the existence of different wind fields has little influence on the inline force
596 and the pitch moment. Referring to Figure 21 and 20, where the surge and pitch motion and

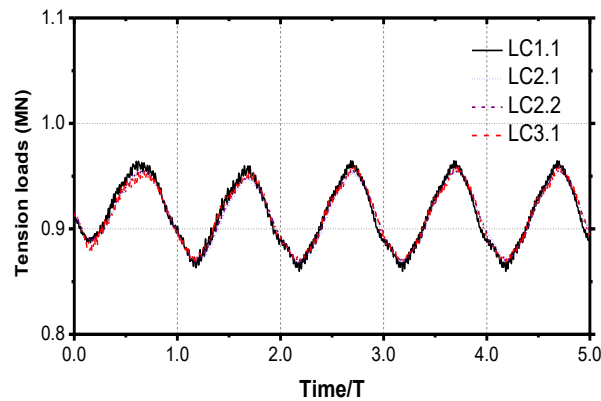


Figure 23 Tension loads of one mooring line (connected with the larboard column) under different wind fields

597 mooring responses are plotted, we can see a similar trend occurs. Looking at the figures, we
598 can deduct that the response amplitude/RAO is nearly identical regardless of whether the wind
599 is uniform, shear or turbulent. Because of this, we can say that the turbulent wind has a
600 negligible effect on the dynamic response of the FOWT substructure in the present study. This
601 could be due to a relatively short-length numerical modelling conducted. It is anticipated that
602 a much longer simulation may capture the low frequency loads induced by the turbulent wind
603 at a very low resonance frequency closer to platform surge natural frequency. This time span
604 for such simulation is around 30-50 periods of the floater natural motion periods, i.e. 900s-
605 6000s, which is hard to be achieved using a high fidelity and computationally expensive CFD
606 solver.

607 Lastly, in contrast to the fluctuation which could be seen previously in both the thrust and
608 power curves in Figure 11, here, we can see no such fluctuation on the curve of the floater. The
609 lack of this fluctuation suggests that the excitation of the incident wave force and the tension
610 of the mooring lines are the dominant factors alongside the dynamic motion responses of
611 FOWT as well as the unsteady tension loading which can be seen in Figure 23. In order to

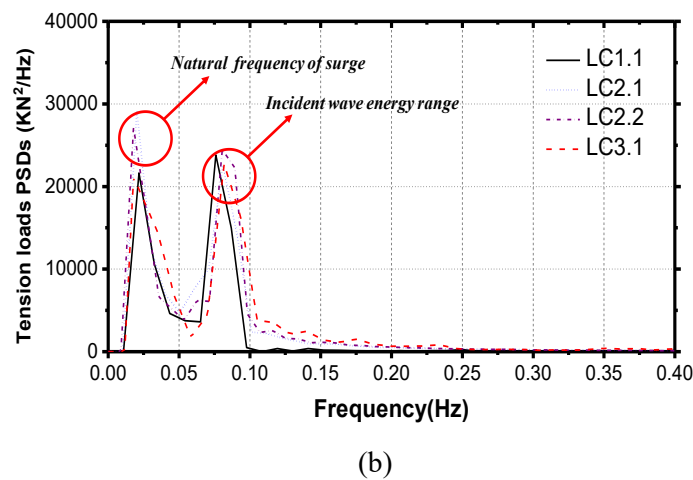
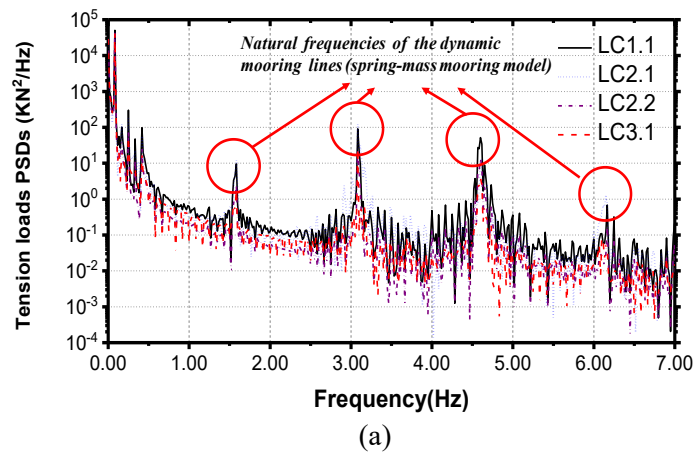


Figure 24 PSDs of tension loads of the mooring line (connected with the larboard column) under different wind fields (a) log plots under the frequency range 0-7Hz, (b) linear plots under the frequency range 0-0.4Hz

612 identify the frequency of the small oscillations observed in Figure 23, we plot the PSDs of the
 613 mooring line tension loads in Figure 24 (a) & (b). From Figure 24 (a), it can be observed that
 614 the peaks inside the circle correspond to the natural frequency of mooring lines. The zoom-in
 615 plot in Figure 24 (b) near the incident wave energy indicate the appearance of two peaks, one
 616 is at the platform surge natural frequency and another is at incident wave frequency.

617 Due to the fact that the hydrodynamic responses of the different wind fields are relatively
 618 similar to each other, the wave elevation CFD contour plots shown in Figure 25 for LC2.1 have
 619 to be plotted within one sampled regular wave period (132s-144s). At the specific time
 620 instances of $t=0.25T$ and $0.75T$, we can see that the floater experiences the maximum and

621 minimum pitch motion, respectively. Looking at the plots, we can clearly see that the wave
622 elevation varies as a direct consequence of a nonlinear wave-structure interaction, such as the
623 wave diffraction or the wave radiation. These interactions are well captured in the present
624 simulation, evidenced by the detailed flow around upstream/side columns.

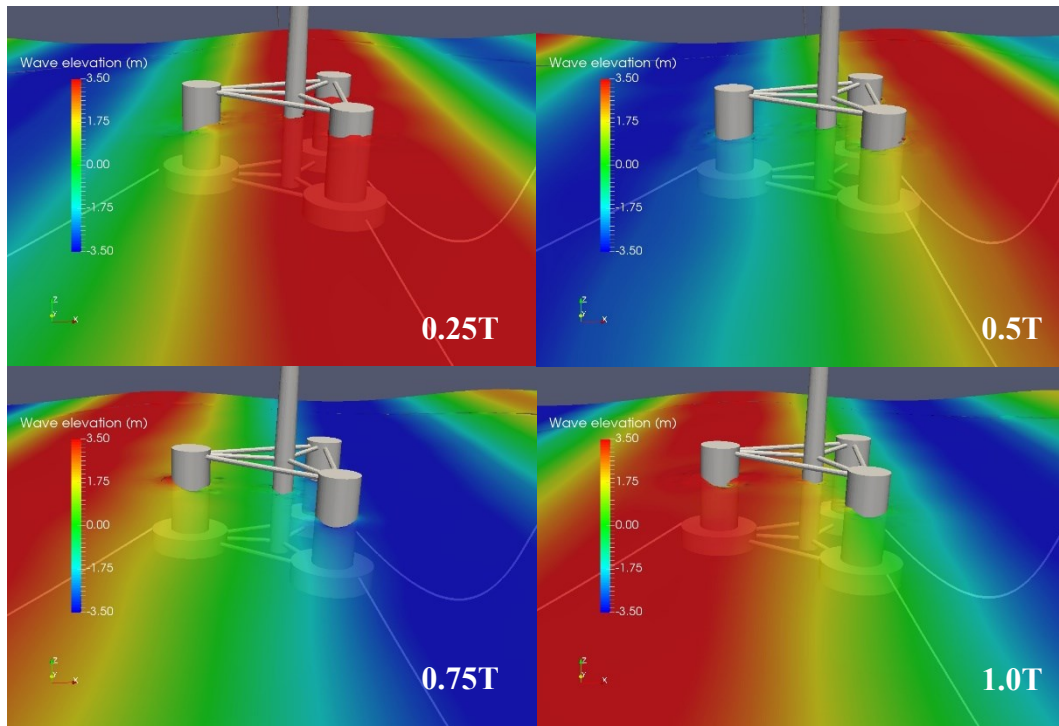


Figure 25 Wave elevation contour plots around the FOWT within one wave period for LCI.1

625 **6 Conclusion and discussion**

626 An investigation was carried out into an OC4 Semi-submersible NREL 5 MW FOWT and its
627 performance under uniform, shear and turbulent wind conditions. This was done by using a
628 blade-resolved CFD tool whilst factoring in the floating platform motion prediction. The
629 investigation started with the generation of wind turbulence based on the Mann wind turbulence
630 model, followed by a validation of the wind spectrum in comparison with the theoretical wind
631 spectrum. Continuing from this, the study led onto the examination into the effects that wind
632 turbulence has on the aerodynamic performance of the turbine i.e, how it influences the turbine
633 and the dynamic responses of the floater.

634 The evidence gathered after comparison between turbulent wind and time-independent wind
635 suggests that the existence of turbulence influences the airflow near the rotor blades, however,
636 its impact on the time-mean flow around the turbine is minimal. The appearance of fluctuations
637 on top of the time-mean thrust and power curve indicate that it is the presence of turbulence
638 causes a larger standard deviation of power, as the value increases compared to when
639 turbulence is absent. In addition, a large wind shear layer thickness results in a sudden drop of
640 the local power in comparison to uniform wind. Despite this, it was found that neither wind
641 turbulence nor wind shear had a significant impact on motion of the floater or the mooring
642 tension loads. These findings are supported by further examinations conducted on the CFD
643 predicted flow field around the wind turbine blades, wake and the wind-wave interactions near
644 the wave-air free surface.

645 Aside from what is mentioned above, there are two points that should be also brought up.
646 Firstly, the frequency of the turbulent wind in this study is quite a bit less than the floater's
647 structural pitch/heave nature frequency of roughly 0.3Hz. Thus, we can predict that the
648 influence of turbulent wind on the floater dynamic responses is limited. Knowing this, we can
649 anticipate that this conclusion will fluctuate if the turbulence frequency is adjusted closer to
650 the FOWT eigenfrequencies, where the resonance of floater may occur. Secondly, the URANS
651 method is used in this study. Due to the nature of Reynolds averaged of this tool, the predicted
652 time-mean values are consistent with other low-fidelity methods. However, we are unable to
653 capture the fine structure of the vortices under the Kolmogorov scale because of the large
654 artificial dissipation embedded in URANS. Because of this, it may weaken our understanding
655 of the vorticity interaction in the turbine wake.

656 **Acknowledgements**

657 This work used the Cirrus UK National Tier-2 HPC Service at EPCC (<http://www.cirrus.ac.uk>)
658 funded by the University of Edinburgh and EPSRC (EP/P020267/1) and ARCHIE-WeSt High
659 Performance Computer (www.archie-west.ac.uk) based at the University of Strathclyde. Yang
660 Zhou thanks China Scholarship Council (CSC) for financial support during his study in the UK.

661

662 Reference

- 663 [1] Roberts, D., 2019, "These huge new wind turbines are a marvel. They're also the future,"
664 Vox, May, 20.
- 665 [2] Larsson, J., Kawai, S., Bodart, J., and Bermejo-Moreno, I., 2016, "Large eddy simulation
666 with modeled wall-stress: recent progress and future directions," *Mechanical Engineering*
667 *Reviews*, 3(1), pp. 15-00418-00415-00418.
- 668 [3] Fang, Y., Duan, L., Han, Z., Zhao, Y., and Yang, H., 2020, "Numerical analysis of
669 aerodynamic performance of a floating offshore wind turbine under pitch motion," *Energy*, 192,
670 p. 116621.
- 671 [4] Thé, J., and Yu, H., 2017, "A critical review on the simulations of wind turbine
672 aerodynamics focusing on hybrid RANS-LES methods," *Energy*, 138, pp. 257-289.
- 673 [5] Lei, H., Zhou, D., Bao, Y., Chen, C., Ma, N., and Han, Z., 2017, "Numerical simulations
674 of the unsteady aerodynamics of a floating vertical axis wind turbine in surge motion," *Energy*,
675 127, pp. 1-17.
- 676 [6] Veers, P., 1984, "Modeling stochastic wind loads on vertical axis wind turbines," 25th
677 Structures, Structural Dynamics and Materials Conference, p. 910.
- 678 [7] Jonkman, B. J., 2009, "TurbSim user's guide: Version 1.50," National Renewable Energy
679 Lab.(NREL), Golden, CO (United States).
- 680 [8] Jonkman, J. M., and Buhl Jr, M. L., 2005, "FAST user's guide," National Renewable
681 Energy Laboratory, Golden, CO, Technical Report No. NREL/EL-500-38230.
- 682 [9] Mann, J., 1994, "The spatial structure of neutral atmospheric surface-layer turbulence,"
683 *Journal of fluid mechanics*, 273, pp. 141-168.
- 684 [10] Gilling, L., and Sørensen, N. N., 2011, "Imposing resolved turbulence in CFD
685 simulations," *Wind Energy*, 14(5), pp. 661-676.
- 686 [11] Chougule, A., Mann, J., Segalini, A., and Dellwik, E., 2015, "Spectral tensor parameters
687 for wind turbine load modeling from forested and agricultural landscapes," *Wind Energy*, 18(3),
688 pp. 469-481.
- 689 [12] Li, Y., Castro, A., Sinokrot, T., Prescott, W., and Carrica, P., 2015, "Coupled multi-body
690 dynamics and CFD for wind turbine simulation including explicit wind turbulence," *Renewable*
691 *Energy*, 76, pp. 338-361.
- 692 [13] Troldborg, N., 2009, "Actuator line modeling of wind turbine wakes."
- 693 [14] Olivares Espinosa, H., 2017, "Turbulence modelling in wind turbine wakes."
- 694 [15] Chivaee, H. S., 2014, "Large eddy simulation of turbulent flows in wind energy," DTU
695 *Wind Energy*.

- 696 [16] Grinderslev, C., Sørensen, N. N., Horcas, S. G., Troldborg, N., and Zahle, F. J. W. E. S.
697 D., 2020, "Wind turbines in atmospheric flow–FSI simulations with hybrid LES-IDDES
698 turbulence modelling," pp. 1-29.
- 699 [17] Li, L., Liu, Y., Yuan, Z., and Gao, Y., 2018, "Wind field effect on the power generation
700 and aerodynamic performance of offshore floating wind turbines," *Energy*, 157, pp. 379-390.
- 701 [18] Doubrawa, P., Churchfield, M. J., Godvik, M., and Srinivas, S., 2019, "Load response of
702 a floating wind turbine to turbulent atmospheric flow," *Applied Energy*, 242, pp. 1588-1599.
- 703 [19] Dolan, D. S., and Lehn, P. W., 2006, "Simulation model of wind turbine 3p torque
704 oscillations due to wind shear and tower shadow," *IEEE Transactions on energy conversion*,
705 21(3), pp. 717-724.
- 706 [20] Cermak, J., and Horn, J., 1968, "Tower shadow effect," *Journal of Geophysical Research*,
707 73(6), pp. 1869-1876.
- 708 [21] Wen, B., Wei, S., Wei, K., Yang, W., Peng, Z., and Chu, F., 2017, "Power fluctuation and
709 power loss of wind turbines due to wind shear and tower shadow," *Frontiers of Mechanical
710 Engineering*, 12(3), pp. 321-332.
- 711 [22] Gould, B., and Burriss, D., 2016, "Effects of wind shear on wind turbine rotor loads and
712 planetary bearing reliability," *Wind Energy*, 19(6), pp. 1011-1021.
- 713 [23] Fang, Y., Duan, L., Han, Z., Zhao, Y., and Yang, H. J. E., 2020, "Numerical analysis of
714 aerodynamic performance of a floating offshore wind turbine under pitch motion," 192, p.
715 116621.
- 716 [24] Lei, H., Zhou, D., Bao, Y., Chen, C., Ma, N., and Han, Z. J. E., 2017, "Numerical
717 simulations of the unsteady aerodynamics of a floating vertical axis wind turbine in surge
718 motion," 127, pp. 1-17.
- 719 [25] Liu, Y., Xiao, Q., Incecik, A., Peyrard, C., and Wan, D., 2017, "Establishing a fully
720 coupled CFD analysis tool for floating offshore wind turbines," *Renewable Energy*, 112, pp.
721 280-301.
- 722 [26] Liu, Y., 2018, "A CFD study of fluid-structure interaction problems for floating offshore
723 wind turbines," PhD thesis, University of Strathclyde.
- 724 [27] Liu, Y., Xiao, Q., Incecik, A., and Peyrard, C., 2019, "Aeroelastic analysis of a floating
725 offshore wind turbine in platform-induced surge motion using a fully coupled CFD-MBD
726 method," *Wind Energy*, 22(1), pp. 1-20.
- 727 [28] Zhou, Y., Xiao, Q., Liu, Y., Incecik, A., Peyrard, C., Li, S., and Pan, G., 2019, "Numerical
728 modelling of dynamic responses of a floating offshore wind turbine subject to focused waves,"
729 *Energies*, 12(18), p. 3482.
- 730 [29] OpenFOAM, 2019, "The OpenFOAM Foundation Website."
- 731 [30] Menter, F., "Zonal two equation kw turbulence models for aerodynamic flows," *Proc. 23rd
732 fluid dynamics, plasmadynamics, and lasers conference*, p. 2906.

- 733 [31] Hirt, C. W., and Nichols, B. D., 1981, "Volume of fluid (VOF) method for the dynamics
734 of free boundaries," *Journal of computational physics*, 39(1), pp. 201-225.
- 735 [32] Jacobsen, N. G., Fuhrman, D.R., Fredse, J., 2012, "A wave generation toolbox for the open-
736 source library: OpenFOAM," *International Journal Numerical Methods in Fluid*, 70, pp. 1073-
737 1088.
- 738 [33] Fan, T., Qiao, D., and Ou, J., "Optimized design of equivalent truncated mooring system
739 based on similarity of static and damping characteristics," *Proc. The Twenty-second*
740 *International Offshore and Polar Engineering Conference*, International Society of Offshore
741 and Polar Engineers.
- 742 [34] Morison, J., Johnson, J., and Schaaf, S., 1950, "The force exerted by surface waves on
743 piles," *Journal of Petroleum Technology*, 2(05), pp. 149-154.
- 744 [35] Von Karman, T., 1948, "Progress in the statistical theory of turbulence," *Proceedings of*
745 *the National Academy of Sciences of the United States of America*, 34(11), p. 530.
- 746 [36] Pope, S. B., 2001, "Turbulent flows," IOP Publishing.
- 747 [37] Madsen, P. H., and Risø, D., 2008, "Introduction to the IEC 61400-1 standard," Risø
748 National Laboratory, Technical University of Denmark.
- 749 [38] Coulling, A. J., Goupee, A. J., Robertson, A. N., Jonkman, J. M., and Dagher, H. J., 2013,
750 "Validation of a FAST semi-submersible floating wind turbine numerical model with
751 DeepCwind test data," *Journal of Renewable and Sustainable Energy*, 5(2), p. 023116.
- 752 [39] Jonkman, J., Butterfield, S., Musial, W., and Scott, G., 2009, "Definition of a 5-MW
753 reference wind turbine for offshore system development," National Renewable Energy
754 Lab.(NREL), Golden, CO (United States).
- 755 [40] Troldborg, N., Sørensen, J. N., Mikkelsen, R., and Sørensen, N. N., 2014, "A simple
756 atmospheric boundary layer model applied to large eddy simulations of wind turbine wakes,"
757 *Wind Energy*, 17(4), pp. 657-669.
- 758 [41] Tian, X., Ong, M. C., Yang, J., and Myrhaug, D., 2013, "Unsteady RANS simulations of
759 flow around rectangular cylinders with different aspect ratios," *Ocean Engineering*, 58, pp.
760 208-216.
- 761 [42] Jonkman, B. J., and Buhl Jr, M. L., 2006, "TurbSim user's guide," National Renewable
762 Energy Lab.(NREL), Golden, CO (United States).
- 763 [43] Quallen, S., and Xing, T., 2016, "CFD simulation of a floating offshore wind turbine
764 system using a variable-speed generator-torque controller," *Renewable Energy*, 97, pp. 230-
765 242.
- 766 [44] Tran, T. T., and Kim, D.-H., 2016, "Fully coupled aero-hydrodynamic analysis of a semi-
767 submersible FOWT using a dynamic fluid body interaction approach," *Renewable energy*, 92,
768 pp. 244-261.
- 769 [45] Kolář, V., 2007, "Vortex identification: New requirements and limitations," *International*
770 *journal of heat and fluid flow*, 28(4), pp. 638-652.

